Nano Energy 136 (2025) 110749

Contents lists available at ScienceDirect

Nano Energy

journal homepage: www.elsevier.com/locate/nanoen

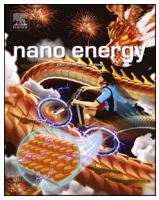

Review

Interfacial lithium-ion transportation in solid-state batteries: Challenges and prospects

Ming Liu [a], Ailing Song [a,*], Xinyi Zhang [a], Jie Wang [a], Yuqian Fan [a], Guoxiu Wang [b], Hao Tian [b,*], Zhipeng Ma [a,c,**], Guangjie Shao [a,c,**]

[a] Hebei Key Laboratory of Applied Chemistry, Hebei Key Laboratory of Heavy Metal Deep-Remediation in Water and Resource Reuse, College of Environmental and Chemical Engineering, Yanshan University, Qinhuangdao 066004, China
[b] Centre for Clean Energy Technology, School of Mathematical and Physical Sciences, Faculty of Science, University of Technology Sydney, Broadway, NSW 2007, Australia
[c] State Key Laboratory of Metastable Materials Science and Technology, Yanshan University, Qinhuangdao 066004, China

ARTICLE INFO

Keywords:
Interfacial lithium-ion transfer
Interfacial resistance
Kinetics design
Solid-state battery

ABSTRACT

Solid-state lithium-ion batteries (SSBs) have gained widespread attention due to their enhanced safety and energy density over conventional liquid electrolyte systems. However, their practical application is hindered by significant polarization during cycling, primarily caused by increased interface impedance. To address the challenges of slow lithium-ion diffusion, optimizing interfacial kinetics has emerged as a key strategy to improve the electrochemical performance of SSBs. However, the mechanisms behind battery failure, especially interface polarization, are not fully understood and require further investigation. This review explores the origins of interfacial polarization, including poor contact, parasitic reactions, and space charge layer, supported by theoretical calculations, experimental data, and advanced characterizations. Then, the latest progress categorized as in-situ solidification, buffer layer, ionic liquid, solid-state electrolytes modification, artificial solid electrolyte interphases, coating layers, dielectric additives, and piezoelectric additives are summarized to elucidate the underlying mechanisms of Li^+ transport across interfaces. Finally, the integration of mechanical behavior with outstanding interfacial engineering is emphasized as a key factor for advancing SSBs performance and stability, providing insights for the development of next-generation lithium-based batteries.

1. Introduction

Lithium-ion batteries (LIBs), as one of the advanced energy storage systems, have been instrumental in shaping both industrial production and everyday life since their commercialization in the 1990s [1]. However, commercial LIBs based on graphite anodes are nearing their theoretical specific capacity limits and fail to meet the increasing demand for higher energy densities [2,3]. Furthermore, the intense exothermic reactions between electrode materials and liquid electrolytes (LEs) during high-current charging and discharging can precipitate rapid temperature increases and significant gas generation within the battery. These phenomena pose serious safety risks, including the potential for battery combustion and explosion [4–6].

The development of SSBs has gained momentum to offer higher energy density and improved reliability, for comprising Li-metal anode, high specific energy cathodes like $Li[Ni_xCo_yMn_{1-x-y}]O_2$ (NCM), $Li[Ni_xCo_yAl_{1-x-y}]O_2$ (NCA), Li_2S, and along with flame-retardant solid-state electrolytes (SSEs) such as oxide, halide, sulfide, and polymer types [7–10]. Recently, extensive research into the transport mechanism of Li^+ in SSEs has led to significant advancements in enhancing the conductivity of various materials to levels comparable to LEs (2 ~ 25 mS cm^{-1} within the range of −20–80 °C) [11–14], further indicating that the slow migration of Li-ions in SSEs is no longer an obstacle to the robust development of SSBs. Thus, the practical realization and broader impact of SSBs on daily life appear highly promising.

Nonetheless, several hurdles must be overcome to transition SSBs from the laboratory to the market. a) Dendrites: Due to the varying lithiation affinities across different crystal facets of the electrodes and

* Corresponding authors.
** Corresponding authors at: Hebei Key Laboratory of Applied Chemistry, Hebei Key Laboratory of Heavy Metal Deep-Remediation in Water and Resource Reuse, College of Environmental and Chemical Engineering, Yanshan University, Qinhuangdao 066004, China.
E-mail addresses: ailing.song@ysu.edu.cn (A. Song), hao.tian@uts.edu.au (H. Tian), mazp@ysu.edu.cn (Z. Ma), shaoguangjie@ysu.edu.cn (G. Shao).

https://doi.org/10.1016/j.nanoen.2025.110749
Received 6 December 2024; Received in revised form 22 January 2025; Accepted 4 February 2025
Available online 7 February 2025

the uneven surface, Li dendrites tend to grow preferentially at highly active region, further leading to a sharp decline in critical current density (CCD) and critical interface overpotential (CIOP) [15]. Moreover, uncontrolled dendrites growth can penetrate SSEs, and subsequently cause battery short-circuiting and degradation in cycle life [16–20]. To address this, various theoretical models have been developed to reveal the nucleation and growth of Li dendrites in SSBs from a (chemo-)mechanical standpoint. Furthermore, strategies for regulating Li metal deposition have also been proposed, including the creation of artificial solid-electrolyte interphases (SEI) [21,22], Li metal alloys [23–25], and buffer layers [26,27]. Given all these attentions, this paper refrains from further elaboration. b) Polarization: Huge polarization not only causes energy wasting but also accelerates aging and structural collapse in SSBs. Detailly, SSBs commonly exhibit small bulk phase resistance but significant interfacial polarization for sluggish carrier transport at the SSEs|electrode interface during electrochemical reactions, typically determined by charge transfer and Li^+ diffusion [28]. Electrons drive key redox reactions at the SSEs|electrode, facilitating the formation of a stable SEI while also posing the risk of triggering undesirable side reactions, such as decomposition or dendrite formation [29]. The localized electron concentration at the interface significantly affects the charge distribution and electric field, modulating the migration behavior of Li^+. While an appropriate electronic conductivity at the interface can reduce interfacial resistance and enhance lithium-ion transport, excessive electron mobility may induce parasitic reactions and compromise interfacial stability. Given the satisfactory electronic conductivity of both cathode and anode in SSBs, optimizing Li^+ transport at the SSEs|electrode interface has emerged as a critical factor for improving reaction kinetics and accelerating the commercialization of SSBs.

In recent years, many exciting and significant progress has been made in developing stable and efficient SSEs|electrode interfaces and decoupling interfacial Li^+ transport dynamics through advanced characterization techniques and computational models. These advances have provided valuable insights into the complexities of interfacial phenomena, which are critical for the performance and stability of SSBs. However, existing reviews tend to focus on specific aspects of these challenges, such as SSEs|electrode interface modification, SSEs design and modification, or non-destructive characterizations. While these studies are informative, systematic overviews addressing broader topics—such as strategies for achieving optimal interfacial impedance and improving Li^+ transfer kinetics—remain underexplored in the current literature [30–33]. Building on existing studies, this review aims to provide a holistic examination of the challenges associated with Li^+ transport at the SSEs|electrode interfaces, focusing on poor contact, parasitic reaction, and space charge layer (SCL) (Fig. 1). And advanced strategies, including in-situ characterization methods and computational simulations, provide insights into the dynamic evolution of interfaces under operating conditions, paving the way for the design of next-generation interfaces. Furthermore, it concludes with a forward-looking perspective on enhancing interfacial Li^+ transport kinetics in SSBs, emphasizing recent breakthroughs in interfacial mechanisms.

2. Dynamics mechanisms and interfacial dilemmas in SSBs

The interface in SSBs constitutes a critical region where key processes—charge transfer, Li^+ migration, and electrochemical reactions—converge. These interfacial dynamics significantly influence the

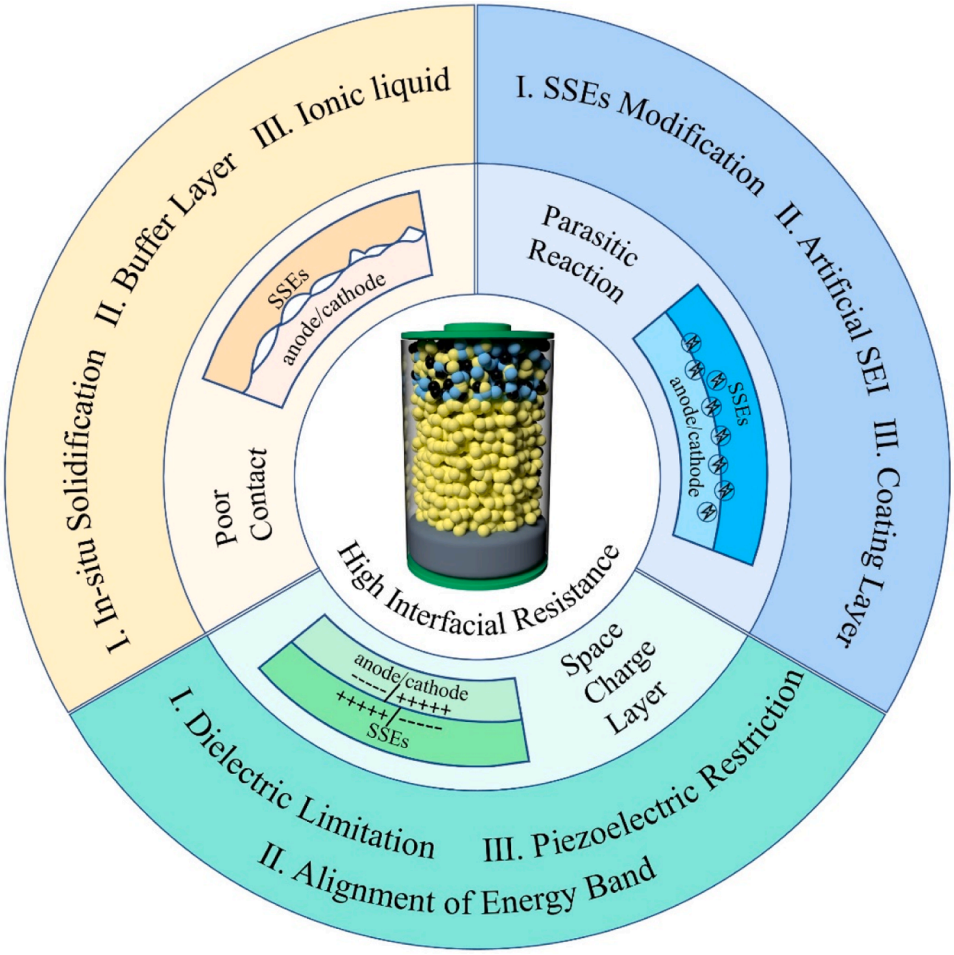

Fig. 1. Schematic of the challenges and solutions for interfacial resistance.

overall performance, energy efficiency, and lifespan by governing ionic conductivity, interfacial resistance, and electrochemical stability. Understanding the complexities is pivotal to mitigating interphase degradation, and achieving long-term cycling stability. And each class of SSEs—oxide, halide, sulfide, and polymer-type—exhibits distinct ionic transport behaviors and interfacial challenges. However, the interplay between bulk transport behavior and interfacial phenomena is multifaceted, requiring an integrated understanding of material properties, interfacial interactions, and operating conditions. For instance, ion migration at the interface is shaped not only by the intrinsic Li^+ conductivity of the bulk SSEs but also by interfacial resistances that develop due to poor contact, interphase formation, and dendritic growth. Optimizing interfaces through approaches like surface modification, buffer layers, and materials with improved chemical compatibility remains vital for advancing high-performance SSBs. Therefore, a thorough exploration of characteristics within the bulk phase of SSEs provides valuable insight into the underlying mechanisms of ion interfacial dynamic.

Oxide-type SSEs, like garnet-structured $Li_7La_3Zr_2O_{12}$ (LLZO), are known for high electrochemical stability and mechanical robustness. Based on crystallographic characteristics, they can be divided into garnet [34], perovskite [35] and NASICON-based structures [36]. Among them, the widely used tetragonal or cubic phase garnet-based SSEs can be written as $Li_{3+x}A_3B_2O_{12}$, where A and B represent high-valence metal cations, such as La^{3+}, Zr^{4+}, Ta^{5+}, Nb^{5+}, etc. In the bulk phase of LLZO, Li^+ randomly occupies the interstitial sites of eight-coordinated [LaO_8] dodecahedra and six-coordinated [ZrO_6] octahedra, specifically the tetrahedral 24d sites and either the octahedral 48 g sites or the more distant 96 h sites from the center. This configuration enables a 3D Li^+ transport pathway (24d - 96 h - 48 g - 96 h - 24d) with ionic conductivity ranging from 10^{-6} to 10^{-4} S cm^{-1} [37]. However, challenges arise from their relatively low Li^+ conductivity and high interfacial resistance, especially in moist air. Besides, their rigid nature also leads to poor wetting at the Li metal interface, resulting in inhomogeneous Li^+ transfer and increased interfacial resistance.

Halide-type SSEs, such as lithium chlorides and bromides, et al., have been developed for a better structural understanding and ion transport mechanisms, offering a unique combination of moderate Li^+ conductivity and high chemical stability against for cathodes [38–40]. Generally, metal-chloride crystal structures consist of hexagonally close-packed or cubic close-packed Li_3MCl_6 (where M represents Y^{3+}, In^{3+}, etc.) or non-close-packed UCl_3-type sublattices (where U represents La^{3+}, Sm^{3+}, etc.). In Li_3MCl_6, Li^+ ions achieve six-coordination with Cl^- ions, facilitating edge-sharing or face-sharing to construct a 3D Li^+ conducting framework [41]. Conversely, UCl_3 structure features a zeolite-like configuration, enabling one-dimensional Li^+ transport along the c-axis [13]. Despite these advantages, their lower mechanical strength and reducibility can introduce issues with dendrite penetration at the SSEs|Li interfaces, compromising long-term stability.

Sulfide-type SSEs, such as $Li_{10}GeP_2S_{12}$ (LGPS) or argyrodite phases, exhibit exceptionally high ionic conductivities (exceeding 10^{-2} S cm^{-1}) and favorable interface properties due to their relatively soft structure [42]. As the most widely applied SSEs, they are categorized into glasses, glass-ceramics, and ceramics-type SSEs [43]. For example, glass or glass-ceramic based xLi_2S-(100-x)P_2S_5 SSEs, synthesized through high-temperature annealing and mechanical ball milling, exhibit Li^+ conductivity primarily governed by the " paddlewheel" effect at low temperatures, in which the lower density of the glassy state (compared to crystalline) accommodates the rotation of complex PS_4 anions, thus enhancing the mobility and migration of Li^+ [44,45]. Crystalline sulfide SSEs are further divided into argyrodite, LISICON, and LGPS types. Typical argyrodite SSEs, like Li_6PS_5X (X = Br, I, Cl, denoted as LPSX), feature a cubic structure with F4-3 m face-centred symmetry, composed of PS_4^{3-} tetrahedra and Li octahedra. The Wyckoff positions 4a and 4d are shared by S^{2-} and X^- anions, while the 16e is filled by S^{2-} anions. Interestingly, in Li_6PS_5I, the 4a position is occupied by I^- anions, attributed to the different ionic radius ratios ($r_{I^-}/r_{s^{2-}}$=1.174, $r_{Br^-}/r_{s^{2-}}$=1.060, $r_{Cl^-}/r_{s^{2-}}$=0.984). Argyrodite SSEs typically exhibit higher Li^+ diffusion coefficient (D_{Li^+}) due to the polarization of S^{2-}, with Li^+ transport paths demonstrated in Fig. 2**A**, where short-range Li^+ transport is achieved through intracage transitions between 48h-24g-48'h and 48h-48"h, and long-range Li^+ transport requires jumping from 48 h_{cage1} to 48 h_{cage2} [46]. However, their chemical instability, especially in humid or oxygen-rich environments, and tendency to form resistive interphase layers (e.g., Li_2S or P_2S_5 decomposition products) present significant challenges for practical applications.

Polymer-type SSEs, conversely, are classified based on molecular structures, such as polyethers, polycarbonates, polyamides, and poly (acrylates). Compared to inorganic SSEs, polymer-type SSEs generally possess superior elasticity and interfacial contact performance, where their remarkable flexibility can mitigate volume expansion and contraction during battery operation [49]. However, unlike the Li^+ hopping paths in inorganic-type SSEs, polymer-type SSEs exhibit lower ionic conductivity due to the sluggish transport of solvated cationic and anion species along the polymer chains. For instance, in poly(vinylidenefluoride) (PVDF)-based SSEs, it is well-known that dissociation occurs when Li salts are too close to polar functional groups. Subsequently, the residual N, N-dimethylformamide (DMF) interacts with Li^+ cations to form $[Li(DMF)_x]^+$ cationic species, which then undergo chain-end transfer through interactions with the electron-rich branched F in the PVDF chains [47,50] (Fig. 2A).

Building on the advantages of combining inorganic and polymer electrolytes, Hybrid Solid Electrolytes (HSEs) have seen significant advancements in recent years. These systems typically consist of inorganic SSEs particles as active fillers (2–50 wt%, no aggregation) and polymer SSEs as the matrix. Depending on the type of fillers, Li^+ transport mechanisms generally fall into two categories (Fig. 2**B**). In systems utilizing SiO_2, LLZO, or other two-dimensional Lewis acid ion conductors, LiTFSI tends to dissociate into ion pairs more readily. The $TFSI^-$ anions are captured by the active filler surface, leaving abundant free Li^+ ions and their solvates for transport. This process simultaneously reduces the crystallinity of the polymer backbone, thereby enhancing ionic conductivity [51]. In contrast, the second category of HSEs features fillers that not only facilitate lithium-ion decoupling on their surfaces but also serve as bulk fast-ion conductors, thereby achieving even higher ionic conductivity [52].

Despite the ionic conductivity of various types of bulk SSEs having been greatly improved, SSEs still face significant polarization and interfacial impedance due to inherently slow Li^+ transport, posing a challenge to the widespread industrial application of SSBs. This is attributed to three distinct factors: interfacial contact loss (Fig. 2**C**), SSEs decomposition (Fig. 2**D**), and SCL (Fig. 2**E**), all of which contribute to slow Li^+ interfacial transport. Since the aforementioned issues are relatively less pronounced in polymer SSEs, this review will primarily focus on inorganic electrolytes to further explore the underlying causes and recent advancements related to these challenges.

2.1. Poor contact

Volume changes in the Li metal anode [53–55] and fragmentation of cathode particles [56–58] are key contributors to void and crack formation, leading to poor contact and slow Li^+ interfacial transport. Void formation at the SSEs|anode interface, akin to bubble formation in boiling liquids, commences with nucleation on the Li metal surface and gradually diffuses inward (Fig. 3**A**). The diffusion rate within bulk Li metal can be likened to the floating rate of bubbles. Due to slow diffusion, vacancies accumulate at the interface and eventually grow into voids, with their morphology and size controllable through current and capacity (Fig. 3**B**) [59]. At low current densities and high capacities, slow vacancy diffusion promotes void nucleation and growth, extending from 2D to 3D cracks. Conversely, a porous morphology emerges at high

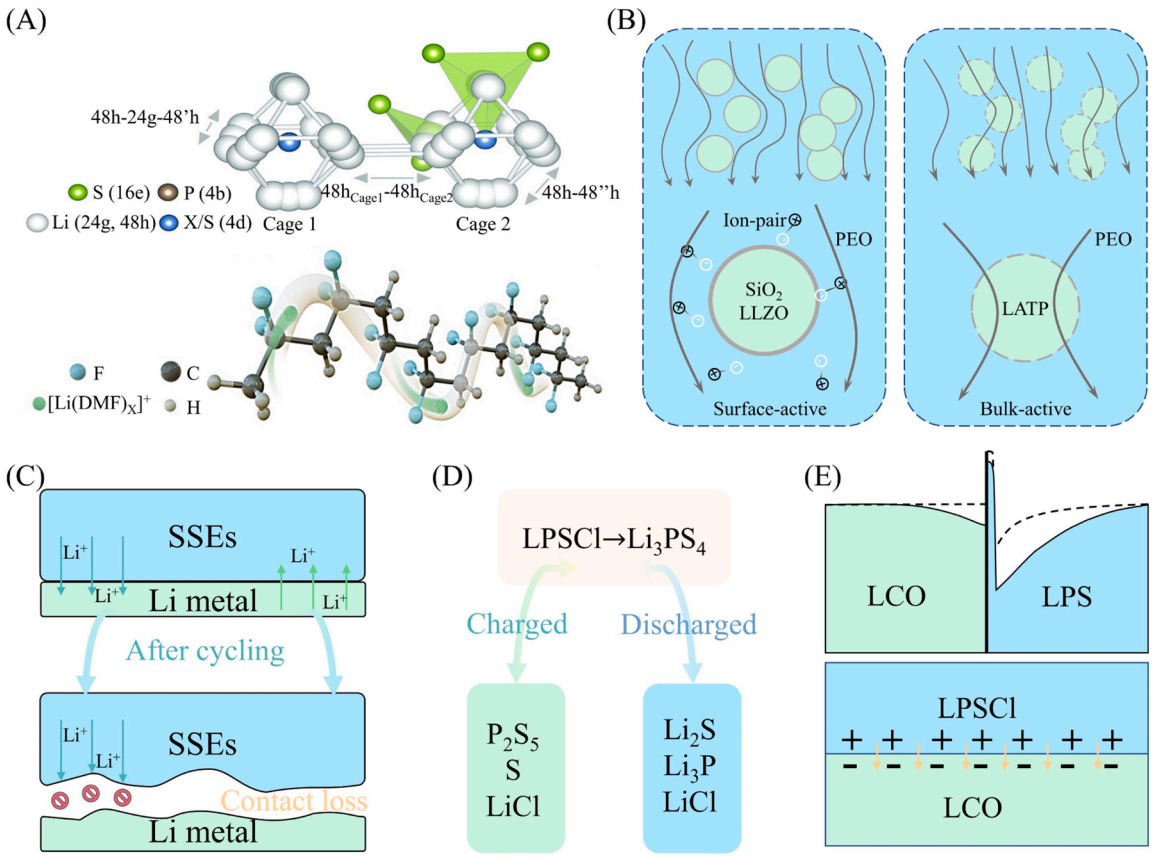

Fig. 2. Transport mechanism of Li^+ in (A) Li_6PS_5X (above) and PVDF (below), and in (B) Surface-active (left) and Bulk-active (right) PEO-based HSEs. [46] Copyright 2019 Royal Society of Chemistry, and Ref. [47] Copyright 2023 Wiley-VCH. (C) Poor contact of the Li|SSEs interface after after cycling. (D) Degradation products of LPSCl: LPSCl will be reduced into Li_2S, Li_3P and LiCl below 1.7 V, and will be oxidized into P_2S_5, S and LiCl while at 2.3 V and above. (E) Proposed Li concentrations in $LiCoO_2|Li_3PS_4$ cathode interface (above) at the initial charging stage and SCL contributed by Li concentration gradient. [48] Copyright 2014 American Chemical Society.

current densities, with void growth behavior proportional to the current density (Fig. 3**C**). FIB-SEM analysis of void aggregation on anode interfaces identifies three distinct regions: stable, transition, and contact failure regions, with poor electrode contact observable under high current density and capacity (Fig. 3**D**).

Furthermore, to elucidate the interplay between current density and stacking pressure on void formation at the Li anode interface, a novel creep/contact electro-chemo-mechanical model has been proposed [60,62]. Using fluid-structure interaction (FSI) theory, Li creep stress distribution is modeled as strain-rate-related creep deformation (Fig. 3**E**). Notably, void formation can be effectively suppressed when the stacking pressure exceeds 12 MPa, even at higher stripping current densities, as sufficient pressure ensures that void formation is dominated by creep stress. Under these conditions, vacancies are transported into the bulk Li before forming new voids, maintaining interface stability (Fig. 3**F**). However, excessive stacking pressure can also cause excessive Li creep, increasing the risk of short circuits during SSB assembly [63]. On the other hand, in the absence of external pressure, vacancies migrate along defects faster than they diffuse into bulk Li, leading to defect growth and crack expansion due to the high self-diffusion barrier. In this case, Li^+ transport dynamics are more limited by contact quality, interfacial physico-chemical properties and transport uniformity. Strategies to optimize the SSEs|electrode interface include introducing high-elasticity polymer SSEs to reduce interfacial stress, incorporating buffer layer to enhance interfacial contact quality, and modifying the surface of SSEs and electrode to expand Li^+ transport pathways, e.g. These approaches will be discussed in detail in the corresponding sections. To summarize, appropriate stacking pressure (e.g., 1–5 MPa) effectively suppresses void generation by lowering the self-diffusion energy barrier [17,64].

Similar to the voids and cracks formation between the Li anode and SSEs, adverse reactions at the cathode|SSEs interface also lead to contact loss due to fissures generation. Layered nickel-rich cathodes, used as high-capacity materials in power batteries, suffer from capacity reduction and micro-cracking due to their inherent mechanical instability and sensitivity to SSEs. When the Ni content exceeds 0.8 ($x > 0.8$), severe anisotropic volume changes caused by phase transitions and residual stress progressively compromise the mechanical integrity of the original particles, exacerbating cracking (Fig. 3**G**) [61]. Moreover, the Li concentration gradient near the interface accelerates micro-cracking, precipitating a steep decline in the capacity [65]. FIB-SEM analysis of cathode degradation after 100 charge-discharge cycles reveals a significant increase in crack width and density in $NCM_{90\ 5\ 5}$, compared to the relatively mild surface degradation of NCM811. This difference is attributed to continuous cracking along grain boundaries and even within particles during cycling, driven by the *H2→H3* phase transition (Fig. 3**H**).

2.2. Parasitic reactions

SSEs degrade upon contact with high-voltage cathode materials (e.g., NCM, LCO) or Li metal due to chemical potential mismatch, leading to the gradual accumulation of side reaction products that form a barrier layer. SEI and cathode electrolyte interphases (CEI) with higher ionic conductivity thereby play an ideal role in preventing side reactions. However, the continuous growth of decomposition products, akin to a tumor, still occurs in the presence of mixed ion-electron conductors or

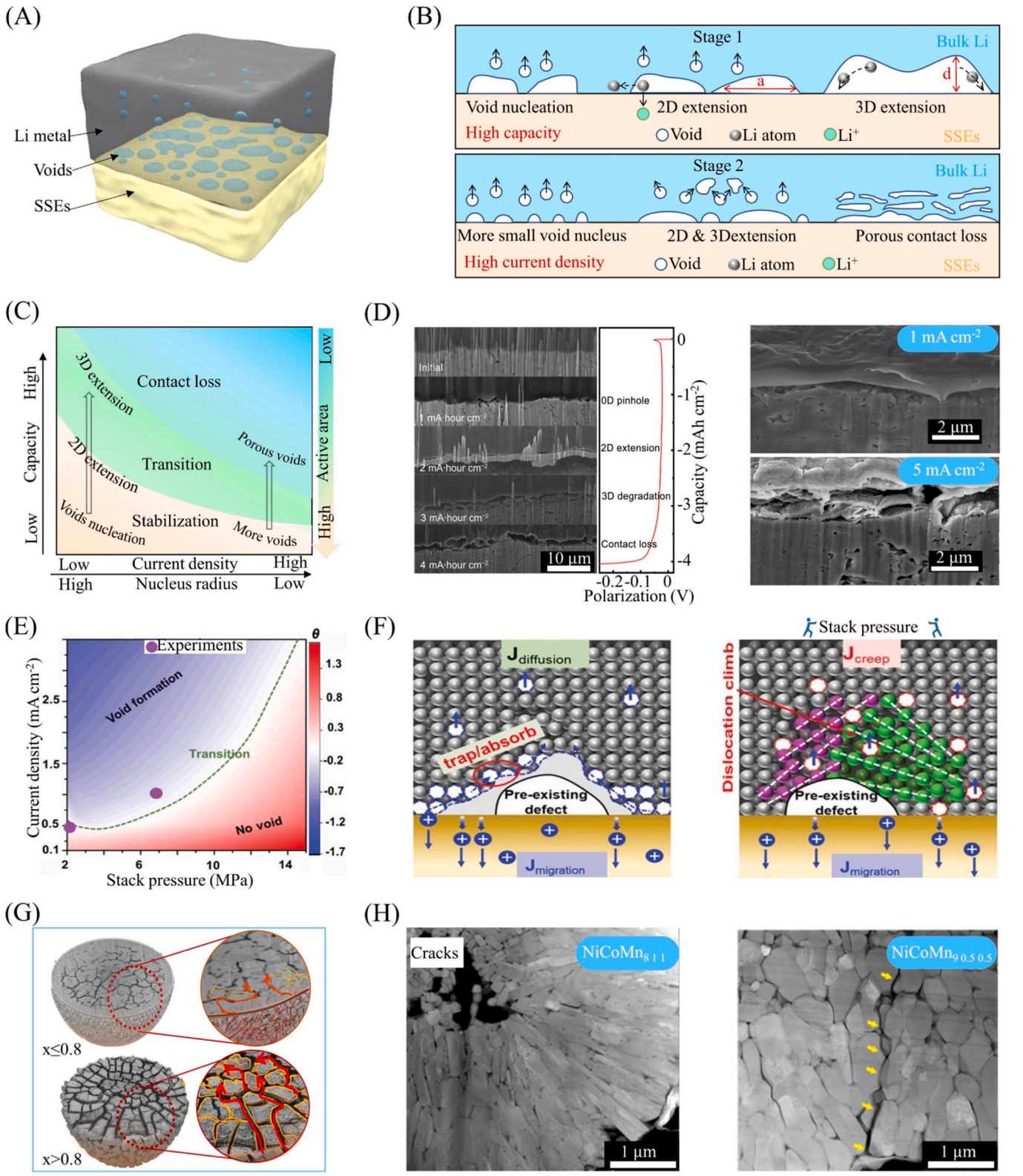

Fig. 3. (A) Formation of void at the anode interface can be abstracted as "bubbles" in the solution. (B) Schematic of different void/gaps evolutions at the anode interface: the nucleated void will preferentially grow horizontally along the anode interface and then extend to 3D with a high capacity; and rapid void growth will be resulted from lots of small nucleuses under an overwhelming current density. (C) The phase diagram reflects the contact loss by the depleting capacity and current density. (D) The evolution of interfacial void/gaps attributed to the depleting capacity and current density is visually illustrated by FIB-SEM images. [59] Copyright 2022 AAAS. (E) The phase diagram of void formation predicted by the applied current density and stack pressure. (F) Void expansion mechanisms in unideal anode interface with and without stack pressure. Specifically, Li vacancy will be trapped by the pre-existing defects and void thereby will form at the interface given the interfacial vacancies are too sluggish to migrate to into the bulk Li (left); however the formation of void will be impeded while applying an enough stack pressure due to the $J_{Li,creep}$ is higher than $J_{Li,migration}$. [60] Copyright 2021 Wiley-VCH. (G) Microcracks schemes of Ni-rich $Li[Ni_xCo_yMn_{1-x-y}]O_2$ cathodes. (H) Dark-field STEM images of the cross-section in discharged NCM_{811} (left) and $NCM_{9\ 0.5\ 0.5}$ (right) cathodes after 100 cycles. [61] Copyright 2018 American Chemical Society.

cracks in SEI/CEI, further leading to capacity decline or failure [66].

Take Li||LPSCl||NCM as an example, Fig. 4**A** illustrates that although ionic pathways are ensured when the cathode material consists of NCM and LPSCl particles, sluggish electron migration hampers cathode-side electrochemical reactions, resulting in slow kinetics and low capacity. The introduction of conductive carbon significantly enhances the performance by facilitating electron transfer through carbon and LPSCl|NCM particles to the triphase interface. However, the formation of an obstructive layer due to irreversible decomposition at interfaces, especially where SSEs and carbon phases contact, severely limits Li^+ transport. While the introduction of conductive carbon increases interface impedance due to side reactions, it still provides a benefit by reducing polarization through proper carbon incorporation. On the Li anode side, the large interface energy of dendrite formation allows the growing Li to further react with SSEs. As a result, SSEs degrade and the formation of unconsolidated SEI layers further increase battery polarization.

The composition of SSEs decomposition products at various voltages can be further analyzed through advanced characterizations like in-situ Raman spectroscopy and in-situ XANES (Fig. 4**B**). Both experimental and computational results have illustrated the electrochemical instability of LPSCl in relation to the voltage window, as shown in Fig. 4**C** [70–72]. Below a potential of 1.7 V (vs. Li^+/Li), LPSCl degrades into Li_3P, Li_2S, and LiCl, while above 2.3 V, oxidation products including P_2S_5, S, and LiCl accumulate at the interface. These by-products congregating at the SSEs|electrode interface disrupt the distribution of reaction currents, exacerbating the isolation of Li^+ conduction channels. Specifically, the irreversible structural transformation of LPSCl into passivation products during initial lithiation is evident from *a* decrease in the peak at 2472.2 eV and an increase at 2473.7 eV in the sulfur K-edge XANES spectra (Fig. 4**D**), with the Li_2S peak intensity remaining essentially unchanged in subsequent cycles. This signifying that the irreversible transformation of SSEs impedes Li^+ cross-interface transport [67]. Additionally, in-situ Raman spectroscopy reveals a weak Li_2S peak at 374 cm^{-1} during cycling, along with peaks at 490 cm^{-1} (2.3 V) and 474 cm^{-1} (4 V), corresponding to S-S stretching in Li_2S_x and S-S bending in S_8. These findings indicate that parasitic reactions lead to excessive interface impedance [68].

Moreover, to quantitatively study the thermal stability of SSEs at the Li anode interface, time-resolved electrochemical impedance spectroscopy (Time-resolved EIS) was employed to track the interface impedance evolution over relaxation time for Li|$Li_{7-x}PS_{6-x}Cl_x$|Li symmetric cells (Fig. 4**E**) [69]. It was observed that the interface impedance significantly increased over extended relaxation times, indicating continuous SSEs decomposition, further clarifying the inability of the decomposition products to form a stable SEI layer.

2.3. Space charge layer

Contrary to prevalent debates over the SCL thickness [73–76] and its potential to hinder Li^+ interfacial transport [77–80], the scientific community remains divided. Typically, a SCL forms between materials with dissimilar chemical potentials, potentially causing an excess or deficit of Li^+ at the SSEs| cathode(anode) interface. However, visualizing Li^+ diffusion behavior within the SCL at an atomic scale remains challenging due to complex factors like carrier distribution, structural disorder, and parasitic decomposition [81,82]. To address this, density functional theory (DFT) has become a pivotal tool for understanding SCL [83–85]. For instance, theoretical analyses reveal the emergence of a pentahedral CoO_4S structure at the $LiCoO_2$ and β-Li_3PS4 interface (LCO (110)|LPS(010)) during the initial charging stage (Fig. 5**A**) [48]. This phenomenon is attributed to sulfur atoms' affinity for cobalt atoms. While the ordered lamellar structure of LPS distorts when Li atoms from LPS are adsorbed atop the CoO_6 octahedra, the ordered atomic configuration of LCO remains intact. Furthermore, the formation energy of Li

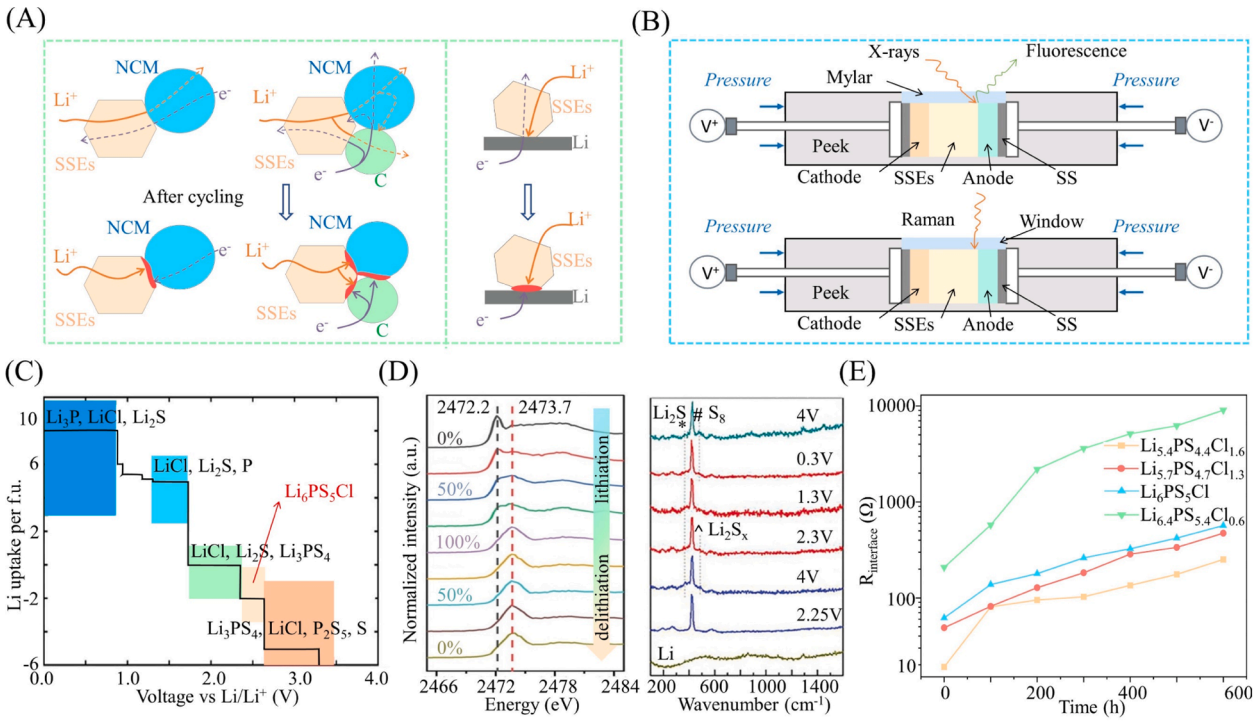

Fig. 4. (A) Schematic of the Li^+- e^- pathways blocked by degradant layers in cathode and anode interfaces. Noting that the carbon additives can not only improve the reaction kinetics but also accelerate the decomposition of SSEs. (B) Schematic of the operando XANES and Raman spectra. (C) Grand potential phase diagram of LPSCl, which process a narrow electrochemical window. [66] Copyright 2020 American Chemical Society. (D) The sulfur K-edge XANES spectra (left) of a carbon-added composite anode at different SOC in the initial cycle, and a rosing peak at 2473.7 eV imply the Li_2S degraded products; and the Raman spectra (right) also indicates the interfacial reaction between the LPSCl and Li. [67] Copyright 2023 Wiley-VCH, and Ref. [68] Copyright 2021 Wiley-VCH. (E) Interfacial impedance of Li|$Li_{7-x}PS_{6-x}Cl_x$|Li symmetric cells as a function of relaxation time. [69] Copyright 2022 Springer Nature.

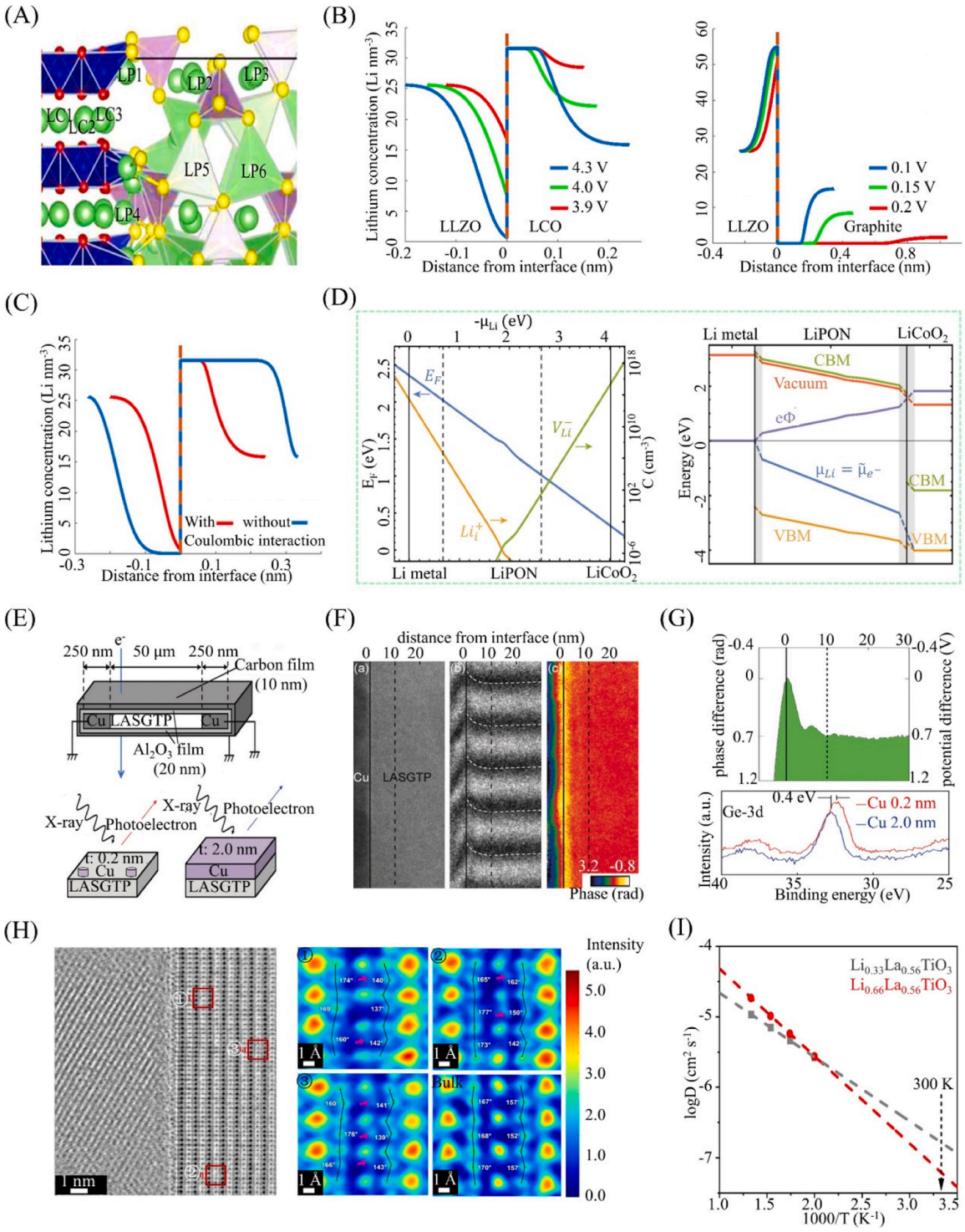

Fig. 5. (A) Possible Li sites with their indices in the LCO(110)|LPS(010) interface structure. The Li, O, P, S and Co atoms were respectively drawn in light green, red, purple, yellow and blue colors. In addition, a largely deformed crystal structure can be found and bring a considerably low Li-vacancy formation energy at LP2 site. [48] Copyright 2014 American Chemical Society. (B) Li concentration at the LLZO|LCO (left) and LLZO|graphite (right) interfaces at different voltages. (C) Li concentration at the LCO|LLZO interface at 4.3 V with and without Coulomb interactions. [83] Copyright 2018 American Chemical Society. (D) Carrier defect concentrations (Li_i^+, orange and V_{Li}^-, blue) as a function of μ_{Li} (left), and the dominant Li carrier changes from cathode to anode can be concluded; thermodynamic potentials and band edges in Li||LiPON||$LiCoO_2$ with open-circuit condition (right). [86] Copyright 2019 American Physical Society. (E) Schematic of the samples prepared for TEM (above) and XPS (below). Noting that an amorphous Al_2O_3 extra-SCL-insulating film and electric shielding carbon film were deposited on the TEM sample, and different thickness of Cu electrodes to calibrate the spectrum shift. (F) Electric potential distribution near the Cu|LASGTP interface obtained from phase-shifting electron holography. (G) Phase and electric potential profiles vertical to the Cu|LASGTP interface (above), and XPS spectra of Ge-3d of the bare LASGTP surface (Correspond to Cu-0.2 nm) and the Cu|LASGTP (Correspond to Cu-2 nm) interface. [87] Copyright 2019 Wiley-VCH. (H) ABF-STEM image of the vicinity of a grain-boundary core (left), and correspond atomic configuration presented in false colors of region I, II and III. (I) Calculated Li diffusion coefficients for $Li_{0.33}La_{0.56}TiO_3$ and $Li_{0.66}La_{0.56}TiO_3$. [88] Copyright 2023 Springer Nature.

vacancies ($E_v(Li_i)$) ranges from 2.62 to 3.27 eV, with Li sites in LP2 exhibit lower $E_v(Li_i)$ values (1.44 eV) and a transfer energy of −1.6 eV to LP1. This is indicative of severe crystal structure deformations, facilitating Li^+ occupation in adjacent LP1 sites. Additionally, electrons accumulate on the LCO side, forming an SCL with an electric field direction from LPS to LCO. This impedes Li^+ migration from the LCO cathode to LPS during charging, leading to an increase in interface impedance.

However, SCL behavior at interfaces, such as LLZO|LCO (graphite), is notably influenced by voltage fluctuations during battery operation (Fig. 5**B**) [83]. Specifically, nano-thick SCL demonstrates resistance below 1 Ω cm^2, but as voltage increases from 3.9 to 4.3 V, Li concentration within the SCL of LLZO|LCO interface diminishes by 35 % and 95 %, while increasing near the LLZO|graphite surface. Models that exclude coulombic interactions between charged defects reveal complexities in Fig. 5**C**, where coulombic interactions significantly reduce the SCL thickness and affect the Li concentration distribution. Remarkably, the nano-thick SCL scarcely impedes Li^+ transport, suggesting that interface impedance is more likely caused by decomposition products or poor contact quality.

The inconsistencies in research findings regarding Li^+ transport within SCL stem from structural disturbances caused by variations in Li^+ concentration distributions, atomic structures, lattice matching and coulombic interaction. Hence, a universally applicable model to accurately predict SCL behavior is urgently needed. Qi et al. developed a model based on thermodynamic driving forces, demonstrating that SCL result from the differential flux between electron migration and Li^+ transfer [86]. As illustrated Fig. 5**D**, charged defects (V_{Li}^-) become the predominant Li carrier at the LiPON|LCO interface, while Li_i^+ occupies the Li|LiPON interface. At the LiPON|LCO interface, V_{Li}^- migrates from LiPON into LCO, whereas Li^+ moves from Li metal into LiPON. Furthermore, *a* Li||LiPON||LCO model was established, where the gray area signifies the SCL at both cathode and anode interfaces. It is observed that due to the Fermi level being deep within the band gap, electrons cannot migrate into LiPON at the Li|LiPON interface, hence the positive electrostatic potential drop ($\Delta\phi$) is predominantly driven by Li_i^+ emitted from the Li|LiPON interface. At the LiPON|LCO interface, the positive $\Delta\phi$ further indicates that fewer Li_i^+ migrate out of LCO than electrons, exhibiting a positive charge. Notably, the negative $\Delta\phi$ signifies that negative charges can accumulate at the LiPON|$Li_{0.5}CoO_2$ interface, primarily due to reduced electron transfers.

In fact, the lack of precise and effective characterization methods often leads to conflicting results regarding the actual role of SCL and the distribution of Li atoms. To experimentally characterize the SSEs|electrode interface potential drop, Y. Nomura et al. [87] developed a novel sample preparation technique that ensures more accurate SCL measurements. Using Cu electrodes paired with $Li_{1+x+y}Al_x(Ti,Ge)_{2-x}Si_yP_{3-y}O_{12}$ (LASGTP), a stable material in air compared to LPSCl and LLZO, the interface was prepared with a charge-shielding carbon layer (10 nm thick) and amorphous Al_2O_3 (20 nm) to prevent additional SCL formation **(**Fig. 5**E)**. Through phase shift reconstruction (Fig. 5**F**) [89], a spatial resolution of 1 nm identified a potential difference of approximately 1.3 V, corresponding to a 10 nm SCL thickness (Fig. 5**G**). Moreover, copper deposition on the LASGTP surface is achieved through electron beam evaporation for further proof of XPS, with its thickness precisely regulated between 0.2 and 2 nm to calibrate spectral shifts induced by the charged state of LASGTP (Fig. 5E). The analysis of Ge-3d spectra across various Cu thicknesses reveals negligible differences, suggesting minimal parasitic reactions at the electrode interface. The establishment of SCL results in a reduction in the inner energy levels of LASGTP by 0.4 eV (Fig. 5G), indicative of a potential drop across the electrode interface and leads to a considerable thickness. Employing annular bright field-scanning transmission electron microscopy (ABF--STEM), Ma et al. [88] has also verified the structural presence of excess Li atoms at the grain boundaries of $Li_{0.3}La_{0.5}TiO_3$ (LLTO), as shown in Fig. 5**H**. Coupling this with Ab initio molecular dynamics (AIMD) simulations (Fig. 5**I**), they deduces an unexpected conclusion that it is the core of the delithiated grain boundary, rather than the negatively charged SCL, that predominantly contributes to significant grain boundary resistance.

3. Kinetic designs of Li^+ interfacial transportation

The kinetic design of Li^+ interfacial transport is a critical factor in enhancing the performance of SSBs. By optimizing the transport mechanisms of lithium ions at the SSEs|electrode interface, improvements can be achieved in charge and discharge rates, energy density, and cycle stability of SSBs, thereby addressing the demand for high-performance solutions in electric vehicles, energy storage systems, and other applications. In the optimization of the kinetic design of Li^+ interfacial transport, the following specific strategies and approaches can be employed: Interface structure optimization, SSEs design, interface modification and alteration, dynamic model and simulation. Specifically, in-situ solidification forms a stable solid layer that enhances both Li^+ transmission efficiency and stability. Additionally, introducing a buffer layer alleviates interface stress and improves compatibility. The use of high ionic-conductivity, low-viscosity Li^+ conductor further reduces transport resistance, while optimizing surface properties enhances the contact between electrodes and SSEs. Modifying the SSEs interface or employing an artificial layer can effectively replace the potentially unstable natural SEI, ensuring more reliable performance. Furthermore, applying protective coatings on the electrode surface isolates it from direct contact with the SSEs, minimizing parasitic reactions. Finally, dynamic modeling and simulation techniques can be utilized to study the impact of the polarized electric field on Li^+ transport, providing valuable insights that guide the optimization of interface design. By integrating these approaches, the performance of SSBs can be significantly advanced, addressing the growing demand for high-performance solutions in electric vehicles and energy storage systems.

3.1. Solutions for intimate contact

In SSBs, poor contact is inevitably associated with high interface impedance, compatibility issues, and interface instability. Inspired by well-wetted LEs|electrodes interfaces, numerous strategies have been developed to enhance contact between SSEs and electrodes, such as in-situ solidification, buffer layers, and ionic liquids, and finally to construct high-speed channels for Li^+ transport at the interface. Utilizing well-designed Li^+ dynamics and the integration of cross-sectional SEM, magic angle spinning NMR (MAS NMR), EIS, and other characterizations, it has been further confirmed that intimate contact between SSEs|electrode interfaces can facilitate the rate of trans-interface transfer.

3.1.1. In-situ solidification

In-situ solidification has been widely applied to improve the wetting contact between SSEs and electrodes due to its scalability for mass production. This typically involves casting a liquid polymer precursor on the electrode surface or melting pre-modified Li metal on the SSEs surface. The precursor solution or molten Li permeated all voids/cracks is then solidified through heating, photoinitiation or cooling, ultimately forms a tight interface (Fig. 6**A, B**).

Benefiting from the unique porous characteristics of covalent organic frameworks (COFs), Guo et al. [91] designed a polymer film with rapid Li^+ conductivity through in-situ polymerization (Fig. 6**C**). Specifically, by infiltrating a DMA@LiTFSI solution into LiCOFs and subsequent annealing and hot-pressing, a solid polymer electrolyte (SPEs) with high flexibility and fast ionic transport was obtained, achieving intimate contact at the SPEs|$LiFePO_4$ (LFP) cathode interface. Further, 2D NMR, 2D grazing-incidence wide-angle X-ray scattering (GIWAXS), and theoretical calculations confirmed that SPEs possess a unique Li^+ transport environment due to the interaction between Li salts and COFs. This

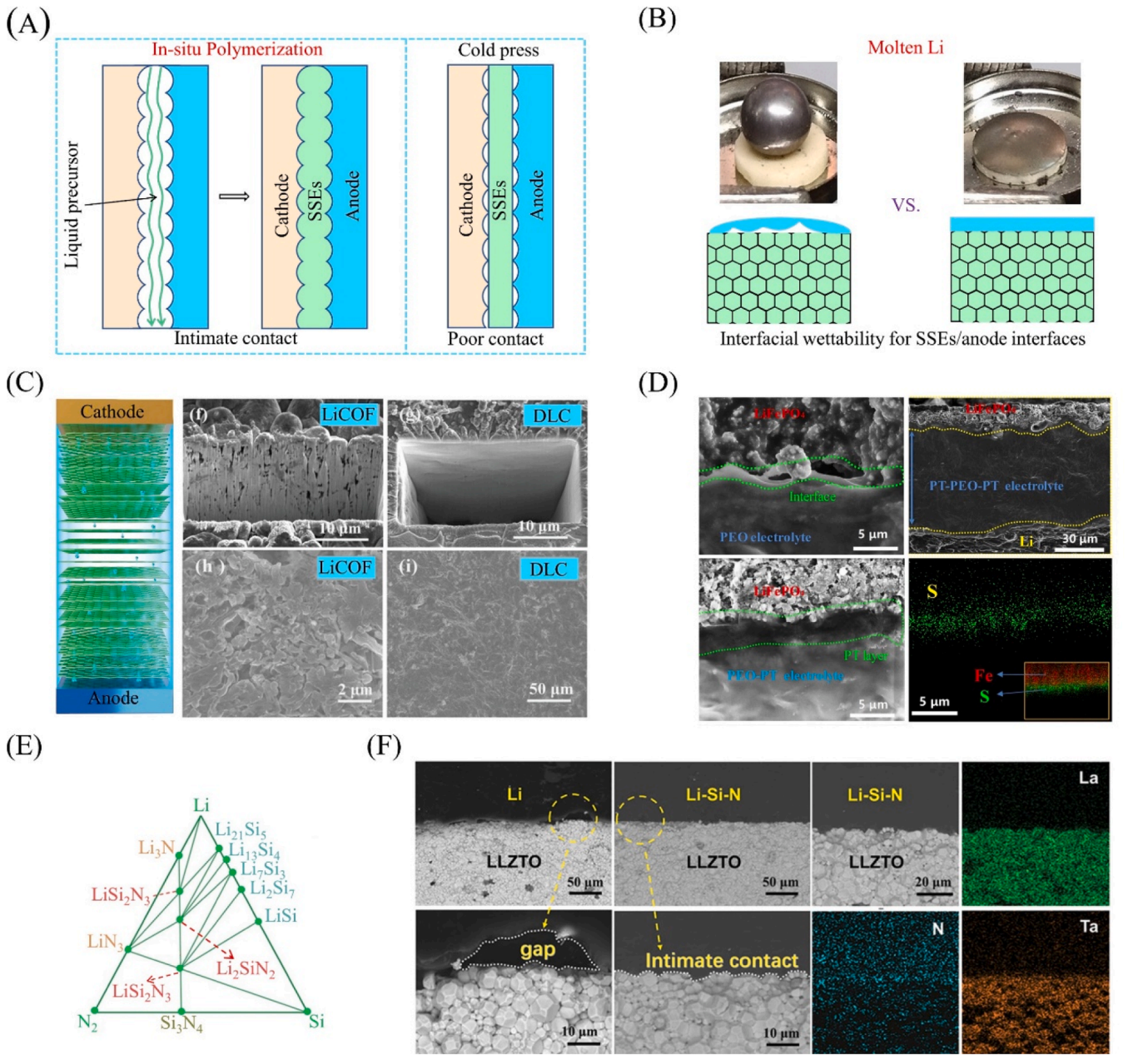

Fig. 6. (A) Schematic of the interfacial differences between in-situ polymerization and cold press. (B) Schematic of the interfacial differences between molten Li|SSEs (left) and modified-Li|SSEs (right). [90] Copyright 2022 Wiley-VCH. (C) Illustration of an SSB with the proposed DLC electrolyte (left), FIB-SEM images of the poor and intimate contact in LiCOF and DLC electrolyte (right). [91] Copyright 2022 Wiley-VCH. (D) Cross-sectional SEM and EDS images of the anode and cathode interfaces with PT-PEO-PT and PEO electrolyte. [92] Copyright 2021 Wiley-VCH. (E) Phase equilibrium diagram of the Li-Si-N system. (F) Cross-sectional SEM and EDS images of the Li|LLZTO and Li-Si-N|LLZTO interfaces. [93] Copyright 2021 Wiley-VCH.

effectively reduced the interfacial impedance of symmetric batteries, enhanced ionic conductivity (σ_{Li^+}) = 1.65 × 10^{-4} S cm^{-1}), and achieved a cycling life exceeding 450 hours. Additionally, Zheng et al. [92] reported the growth of a dual ion-electron conductive polymer layer (named PT-PEO-PT) at the SPEs|electrode interface. In Fig. 6**D**, Li|| PT-PEO-PT||LFP batteries demonstrated more compact contact and good connectivity at the interface, with the distribution of S also confirming the uniform presence of PT. After 300 cycles, the interface resistance of the battery decreased from 3912 Ω to 360 Ω, indicating the significant advantages of PT in improving interface stability and Li^+ transport. Inspired by vertical channel structures, Nie et al. [94] proposed a concept for low-tortuosity LFP cathodes and achieved outstanding mechanical flexibility and interface compatibility of SPEs through in-situ polymerization.

Furthermore, garnet-based SSEs, such as LLTO and $Li_{6.4}La_3Zr_{1.4}Ta_{0.6}O_{12}$ (LLZTO), have been extensively studied for their excellent stability and outstanding Li^+ transport performance [95–97]. However, due to the high rigidity of garnet-based SSEs, the widely accepted cold-pressing strategy still fails to ensure uniform Li^+ flux distribution and stable transport kinetics at the interface during battery operation [98,99]. The low melting point characteristic of Li metal (180 °C) makes it possible to transform the interface from poor solid|solid contact to compatible wetting liquid|solid contact. Thus, numerous attempts [100–102] have been made to modify Li metal and transform SSEs from lithium-phobic to lithium-philic, thereby enhancing interface wettability and Li^+ cross-interface transport capability. Du et al. [93] constructed a satisfactory anode interface by mixing a small amount of Si_3N_4 (1 wt%) with molten Li. The ternary phase diagram results of

Li-Si-N in Fig. 6**E** show that the alloy anode consists of reaction products of Si_3N_4 and Li, composing of Li_3N, $LiSi_2N_3$, and Li_xSi. DFT calculations further suggest that the introduction of Si_3N_4 not only reduces interface formation energy but also lowers surface tension, facilitating rapid Li^+ migration. The improved interface contact, as shown in Fig. 6**F**, demonstrated a critical current density of up to 1.8 mA cm^{-2} and an ultra-low interface resistance of 1 Ω cm^2 at the Li|LLZTO anode interface at 25 °C, indicating accelerated interface Li^+ transport kinetics. Additionally, a composite Li anode (CLA) was designed by adding $LiNO_3$ to molten Li, effectively improving interface wettability and promoting Li^+ diffusion capability due to the uniform dispersion of ionic conductors Li_3N and LiN_xO_y [101]. DFT calculations further revealed the extremely low interface formation energy of LLZTO|LiN_xO_y and LLZTO|Li_3N, consistent with the actual ultra-low interface resistance (1.73 Ω cm^2). Thanks to the enhanced interface Li^+ transport kinetics, the LFP||LLZTO||LNO10 (Li: $LiNO_3$ mass ratio of 10:1) full cell achieved a high capacity retention rate of 80.0 % after 500 cycles at 1 C. A dense contact mixed conductive CLA was also prepared at the anode|SSEs interface through in-situ conversion using the reaction between molten Li and AlF_3 [90]. The robust interaction between CLA and LLZTO forms a high-speed Li^+ transport channel, facilitating uniform Li deposition and optimal utilization. After cycling for 1500 hours, the L4AF= |LLZTO|| L4AF (Li: AlF_3 mass ratio of 4: 1) symmetric battery exhibited only *ca.* 50 mV of overpotential at 0.3 mA cm^{-2}. These previous studies indicate that constructing composite Li anodes with high electronic/ionic conductivity and excellent wettability will present a significant

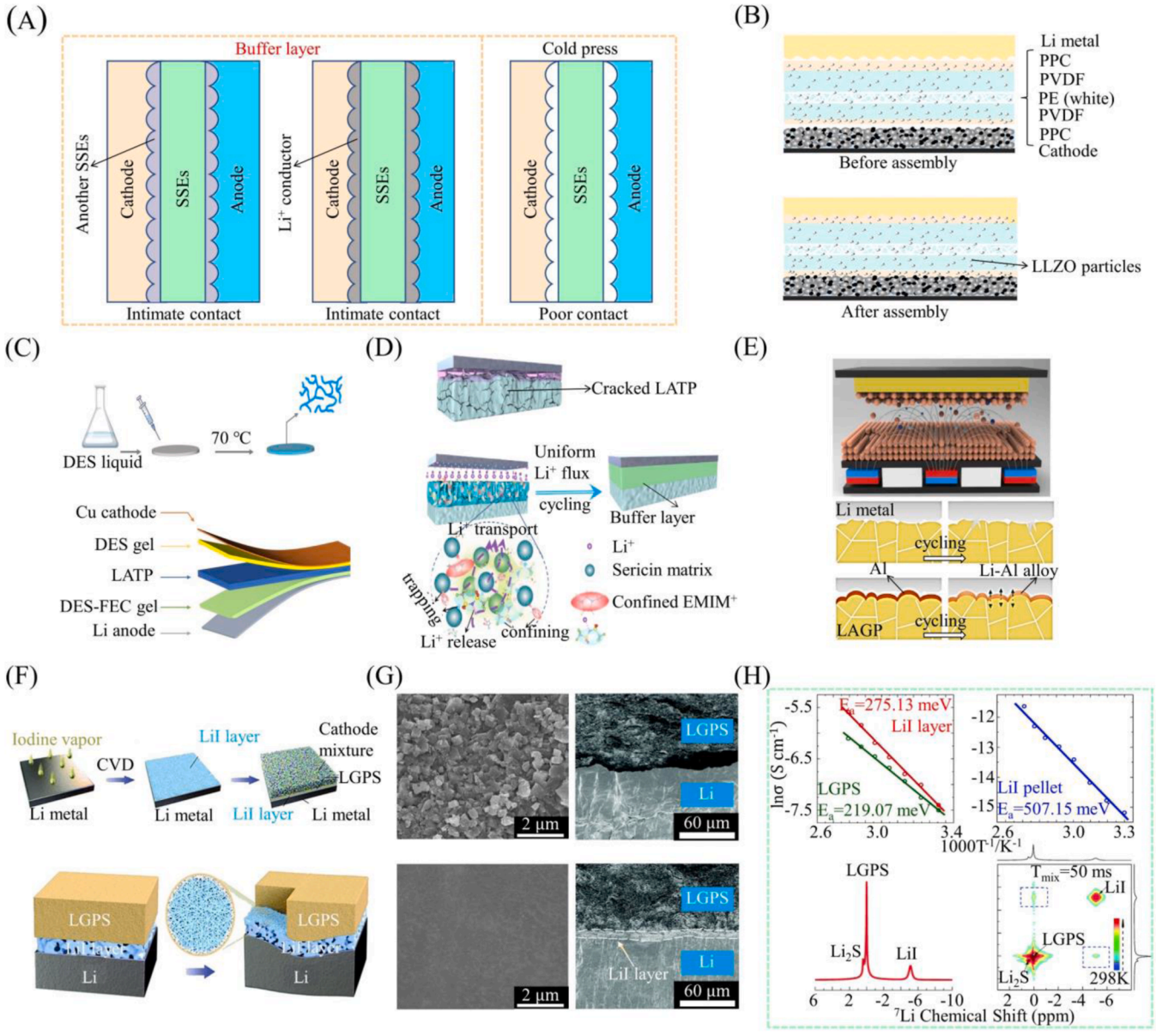

Fig. 7. (A) Schematic of the interfacial differences with and without Li^+ conductive buffer layers. (B) Constitutions of the SSBs assembly with LSCE buffer layer. [108] Copyright 2021 IOP Publishing. (C) Schematic of the Li-Cu SSBs sandwiched with DES gel. [109] Copyright 2023 Wiley-VCH. (D) Schematic of failure mechanism in anode interface with (below) and without (above) SPF during cycling. [110] Copyright 2022 Elsevier. (E) Schematic of magnetron sputtering of nanoscale of Al buffer layer on the LAGP surface. [111] Copyright 2022 Springer Nature. (F) Schematic of the preparation (above) and well compatibility (below) of the LiI layer on the Li metal surface. (G) Surficial SEM images of LAGP and AIOC-LAGP (left), and Cross-section SEM of the anode interface with (below) and without (above) LiI buffer layer after 50 cycles. [112] Copyright 2021 Elsevier. (H) Arrhenius plot of the Li||LGPS||Li, Li||LiI||LGPS||LiI||Li cell and commercial LiI (above), and 1D ^{7}Li MAS spectrum and ^{7}Li 2D-EXSY spectrum of the LGPS-LiI mixture at 298 K for 50 ms mixing time (below). [113] Copyright 2022 Royal Society of Chemistry.

enhancement in reducing interface resistance and promoting interface Li^+ transport.

3.1.2. Buffer layer

Uneven Li deposition often leads to the creation of voids and gaps at the interface due to significant volume changes. These phenomena result in high interfacial impedance and pronounced polarization, posing a significant bottleneck to the application of SSBs. The development of buffer layers to refine the SSEs|electrode interface has been identified as a promising approach (Fig. 7**A**). Recent breakthroughs, facilitated by advanced techniques such as atomic layer deposition (ALD), chemical vapor deposition (CVD), vacuum evaporation, magnetron sputtering, and molecular layer deposition, have enabled the integration of metal oxides [103], alloy metals [104,105], and other Li^+ conductors [106,107]. These advancements not only extend the electrochemical window of SSEs but also enhance interface stability and ensure efficient Li^+ interfacial transport.

Drawing inspiration from the solid-state polymer|ceramic|polymer sandwich structure proposed by Goodenough et al. [114]. Chen et al. [108] discovered that employing poly(propylene carbonate) (PPC), known for its porosity and facile internal rotation structure, as a buffer layer significantly diminishes the activation energy (E_a) for Li^+ migration. The PVDF-LLZO|PPC-LLZO multilayer SSEs (LSCE) form an effective contact with the interface through in-situ gel wetting, thereby reducing interfacial impedance (Fig. 7**B**). Additionally, the reaction of PPC with Li metal generates a robust SEI layer, enhancing interface stability, suppressing dendrite growth, and preventing the formation of voids/gaps left by depleted Li metal. Wang et al. [109] introduced a sandwich SSE for Cu-Li SSBs, incorporating deep eutectic solvent (DES) gel and DES gel with 10 wt% fluoroethylene carbonate (FEC) additive as buffer layers on both sides of $Li_{1.4}Al_{0.4}Ti_{1.6}(PO_4)_3$ (LATP) (Fig. 7**C**), effectively mitigating the shuttle effect of Cu ions. However, the preparation of these polymer-based buffer layers often involves various harmful substances (e.g., DMF).

Natural biomaterials, owing to their environmental friendliness, sustainability, abundant availability, and low costs, thereby have garnered widespread attention [115]. Lei et al. [110] stabilized the anode interface with a compatible silk fibroin film (SPF, Fig. 7**D**) serving as a bio-buffer layer. The SPF, firmly adhering to the SSEs surface, offers numerous lithium-friendly sites (e.g., -COOH and -CO-NH with electron-donating C═O functional groups) to attract and transport Li cations, thereby enhancing interfacial transport dynamics [116–118]. The introduction of molecular electrostatic potential (MESP) analysis also revealed that the weak intermolecular interactions along the SPF main chain are insufficient to securely anchor $TFSI^-$, whose short-range movement resembles local migration within an ion-gel crosslinked network, leading to a reinforced and adhesive composite interlayer between the Li metal and LATP SSEs.

Furthermore, the exploration of lithiophilic metals [119,120], metal nitrides [121,122], and metal oxides [123,124] as buffer layers has gained attention, aimed at enhancing the SSEs|electrode interface. A magnetron-sputtered ultra-thin Li-Al buffer layer (Li-Al alloy layer) on the LAGP surface has been shown to accelerate Li atom diffusion (Fig. 7**E**) [111], thereby augmenting the cycling stability and rate performance of SSBs. Li and his team also deployed a viscous anion-immobilized oligomer ionic conductor (AIOC) as a buffer layer for $Li_{1.5}Al_{0.5}Ge_{0.5}P_3O_{12}$ (Al-LAGP), thus minimizing the interfacial resistance of symmetric batteries [112] (Fig. 7**G**). Duan et al. [113] fabricated a dense, intertwined, and mechanically robust LiI crystal layer on the Li|SSEs interface using the CVD method (Fig. 7**F**), preventing contact failure and the formation of voids/gaps at the Li||LiI||LGPS||LiI||Li interface during cycling (Fig. 7 G). Notably, while the introduction of LiI results in a slightly higher E_a and interfacial resistance, it still serves as an efficient Li^+ transport bridge between Li and LGPS (Fig. 7**H**), enabling stable cycling of a Li||LiI||LGPS||S full cell for 150 cycles.

In summary, the large-scale fabrication and cost control of buffer layers based on inorganic salts or alloys remain immature. Therefore, the development of abundant, low-cost, and easily prepared fast ion conductors (e.g., two-dimensional materials such as kaolinite and lithium manganese phosphate) holds significant promise for future applications. When polymer-based or hybrid lithium-ion conductors are used as buffer layers, it is challenging to control the total thickness of SSEs within 10 μm. Current casting techniques may be replaced by methods such as spraying, self-assembly, or interfacial polymerization in the future.

3.1.3. Ionic liquid

In the realm of HSEs, the incorporation of ionic liquids (ILs) emerges as a pivotal strategy for enhancing Li^+ diffusion and reducing crystallinity in SPEs. ILs, with their unique attributes including low vapor pressure, non-flammability, high ionic conductivity, and wide electrochemical window, are adept at permeating contact interfaces between solid particles, thereby significantly lowering interfacial impedance. The strategic deployment of minimal IL quantities into interfacial voids, either formed during cold-pressing or throughout charge-discharge cycles, effectively diversifies Li^+ transport pathways from a singular solid|solid interface to a complex solid-liquid-solid or solid-solid interface, as illustrated in Fig. 8**A**. The methodologies for IL-modification of SPEs are broadly categorized into three main approaches: physical blending, immersion and swelling, and in situ polymerization [125–128]. Among these, physical blending is widely favored due to its simplicity, allowing for IL-SPEs with up to 60 wt% IL content. Although in situ polymerization may introduce impurities, such as unreacted monomers or initiators, it maximizes the avoidance of organic solvents and enhances interface wettability.

To elucidate the Li^+ transport mechanism at the interface of HSEs, Liu et al. [129] introduced two representative ILs, EMIM-TFSI (1-ethyl-3-methylimidazolium bis(trifluoromethylsulfonyl)imide) and PP13-TFSI (1-methyl-1-propylpiperidinium bis(trifluoromethylsulfonyl)imide), into LiTFSI-PEO-LPSCl HSEs. Their findings revealed a stark absence of 7Li 2D-EXSY cross-peaks in HSEs without ILs, indicating exceedingly slow Li^+ diffusion at the interface. Conversely, the presence of PP13 resulted in distinct 7Li 2D-EXSY cross-peaks in HSE-PP13, signifying enhanced Li^+ diffusion at the organic-inorganic interface. Fig. 8**B** further delineates the diffusion mechanism of Li^+ in HSEs containing the PP13-TFSI additive, where Li^+ is transported along the PEO main chains soaked with PP13 IL and LPSCl particles. Yu et al. [130] observed that the introduction of specific ILs could concurrently promote Li^+ transport in bulk PEO|LLZO HSEs and at the SSEs|electrode interface. As demonstrated in Fig. 8**C**, PEO|LLZO@[Py14]TFSI ($P12LP_x$, where x denotes the mass fraction of [Py14]TFSI additive) exhibited an incremental D_{Li^+} with a rising [Py14]TFSI content. However, IL leakage in HSEs was noted when x exceeded 17.5 wt%. Simultaneously, HSEs modified with [Py14]TFSI demonstrated superior interface compatibility when applied to full batteries assembled with NCM811 and Li metal, in comparison to [BMIM]TFSI and [EMIM]TFSI. Generally, ILs addition markedly reduces interfacial impedance while enhancing the thermal stability and Li^+ conductivity of SSEs [13,132].

Grafting polymeric ionic liquids (PILs) onto polymer molecules is another innovative strategy to enhance Li^+ interfacial transport kinetics, gaining attention due to their remarkable chemical affinity, high ionic conductivity, excellent interface compatibility, and electrochemical stability. Fu et al. [131] introduced a plasticized SPEs based on PIL and IL, composed of poly(dimethyl diallylammonium bis(fluorosulfonyl)imide) (PDADMAFSI), a plasticizer N-butyl-N-methylpyrrolidinium bis(trifluoromethylsulfonyl)imide (PYR13FSI) and LiFSI salt. Characterized by an oxidation resistance exceeding 5.0 V and a high ionic conductivity of 0.8 mS cm^{-1}, the SPEs not only facilitated uniform Li metal deposition and dissolution during charge-discharge cycles but also exhibited exceptional flame resistance (commencing decomposition at about 300 °C), as shown in Fig. 8**D**. XPS spectra in Fig. 8**E**, revealed the formation of LiF-rich interphases, effectively inhibiting dendrites

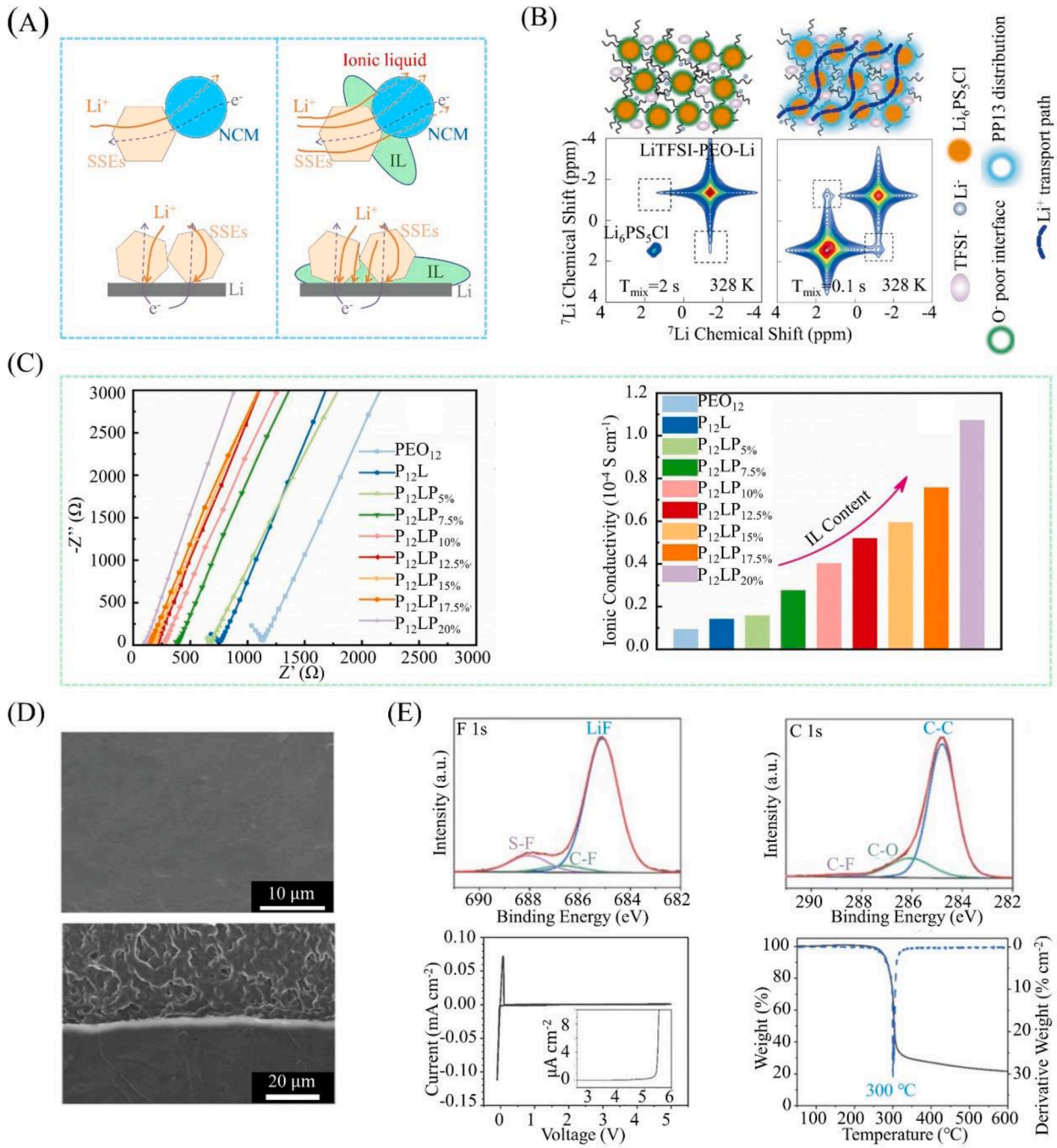

Fig. 8. (A) Schematic of the transport path of Li^+ with and without the addition of IL, and an intimate contact can be performed with a little additive of IL. (B) Different mechanisms for Li^+ migration in HSEs with and without PP13-TFSI IL additives (above), and the corresponding Li^+ transport spectrums by ^6Li 2D-EXSY characterizations (below). [129] Copyright 2022 Springer Nature. (C) Impedance (left) and calculated ionic conductivity of $P_{12}LP_X$ HSEs (right) with different contents of IL at room temperature. [130] Copyright 2023 Elsevier. (D) Surficial SEM image of the Li metal (above) and cross-section SEM image of the anode interface in the symmetric cell after cycling for 200 h at 0.1 mA cm^{-2}. (E) F 1 s and C 1 s XPS spectrum of the cycled Li electrode (above), and CV curve and TGA analyses of the PIL-IL SSEs (below). [131] Copyright 2022 Wiley-VCH.

penetration and consolidating the stability of both anode and cathode interfaces [133,134].

Despite these advancements in improving interface contact capabilities, it should be noted that these methods may introduce additional interfacial resistance caused by corrosion between IL and electrode/SSEs. From the perspective of molecular orbital design, the electronic properties of IL can be tailored to suppress side reactions [135,136]. For instance, lithium metal, with its low Fermi level, may reduce the LUMO of IL upon interaction, leading to the byproducts formation. Introducing substituents with higher electron negativity (e.g., fluorinated groups) or rigid aromatic ring structures can elevate the LUMO of IL, minimizing reductive decomposition. Similarly, lowering the HOMO energy level can also enhance the oxidative stability of IL. Furthermore, AIMD simulations and high-throughput screening can further identify molecular structures that form weak interactions with electrode surfaces, thereby simultaneously achieving high ionic conductivity and interfacial stability.

3.2. Inhibition for parasitic reaction

In addition to establishing compatible and close contacts between SSEs and electrodes, several approaches have been developed to construct rapid channels for Li^+ transport at the interface, including SSEs modifications, artificial SEI on anodes, and coatings on cathodes. These strategies not only regulate the deposition behavior of Li^+ and suppress dendrite formation but also mitigate battery failure arising from continuous SSEs decomposition, thereby ensuring the reliable operation of SSBs.

3.2.1. SSEs modification

A significant challenge faced by inorganic SSEs is their high sensitivity to humid air, which accelerates side reactions leading to phase changes and structural degradation. This irreversible damage destroys the original Li^+ transport structure and reduces ionic conductivity. Conversely, SPEs, despite their superior flexibility and stretchability, are limited in commercial batteries due to their low ionic conductivity ($\sigma_{Li^+} < 10^{-4}$ S cm^{-1}) and sluggish interfacial Li^+ transport. To overcome these limitations, SSEs modification has emerged as a prevalent strategy for regulating Li^+ transport and effectively preventing parasitic reactions by regulations at the surface, composition, and structural levels [35].

As a typical representative of inorganic SSEs, LATP suffers from (electro)chemical incompatibility, which restricts its electrochemical window and results in elevated interface impedance. To develop a highly compatible LATP superionic conductor, Zhu et al. [137] ingeniously in-situ constructed a 3D organic/inorganic BNRA composite layer (200 nm thick) on the surface of LATP by spraying a solution consisting of carboxymethyl cellulose, commercial h-BN, and acetone solvent. Due to the highly lithium-philic nitrogen atoms in the BNRA, this layer establishes a robust Li^+ conductive interface (Fig. 9**A**). When compared to Li||LATP||Li symmetric cells, symmetric SSBs with BNRA-LATP demonstrated satisfactory thermal stability at 264.9 ℃ (Fig. 9**B**). However, polymer electrolyte SPEs typically possess a wider electrochemical window and thermodynamic stability but are prone to degradation, such as PVDF-HFP, which undergoes uncontrollable defluorination reactions and solvent decomposition during battery cycling, leading to the formation of an unstable porous SEI and hindering Li^+ transfer at the interface. To address this issue, a 2D fluorinated graphene (FG) reinforced PVDF-HFP-LiTFSI SPEs (dubbed FPH-Li) was developed [138]. The introduction of FG not only bolsters mechanical properties but also enhances Li^+ transport at the interface and equalizes Li^+ flux (Fig. 9**C**). More importantly, the fluorine groups on the surface of FG form a thermodynamically stable and dense modification layer, ensuring that parasitic reaction by-products like LiF scarcely accumulate at the anode interface, thus preserving the structural integrity of SPEs at the negative electrode interface (Fig. 9**D**).

In addition, it is acknowledged that mixed ionic-electronic conducting interfaces, arising from side reactions, not only promote dendrite formation but also lead to continuous SSE degradation and increasing interface impedance. Thereby, a multi-layered configuration of Cl-rich $Li_{7-x}PS_{6-x}Cl_x$ was proposed to mitigate these shortcomings [27]. Moreover, Zeng et al. discovered that the capability to suppress unfavorable Li deposition and the (electro)chemical stability of the interface are heavily influenced by the chlorine content [73]. With an increasing Cl doping content from 0.6 to 1.6, the SSEs retained the argyrodite structure and appeared a declining cubic lattice parameter from 9.890 Å to 9.788 Å (Fig. 9**E**). Additionally, XPS revealed a reduction in the mixed ionic-electronic conducting interface at the anode (e.g., PS_4^{3-}, Li_2S, Li_3P, and Li_2S_n) with an increase in chlorine content (Fig. 9**F**). It is shown that Cl in $Li_{7-x}PS_{6-x}Cl_x$ preferentially aggregates at grain boundaries and progressively migrates to the Li|SSE interface during cycling, forming a dense and uniform LiCl-dominant layer (Fig. 9**G**), thus preventing SSE decomposition and enhancing the overall performance of the battery.

3.2.2. Artificial SEI

An ideal SEI typically boasts high Li^+ conductivity and exceptional mechanical properties. These features not only enhance Li deposition behavior and inhibit dendrite growth but also enable swift Li^+ transport while mitigating degradation of SSEs. To address unstable interfaces caused by side reactions, an in-situ electrochemical reduction technique was utilized to engineer a nano-composite SEI layer comprising LiF, -NSO_2-Li, Li_2O inorganic salts, and LiO-$(CH_2O)_n$-Li elastic organic salts (Fig. 10**A**) [139], achieving a stabilized anode interface. This engineered SEI layer exhibits remarkable (electro)chemical stability, minimal interface resistance, and high compatibility with LGPS.

Moreover, certain inorganic lithium compounds (e.g., LiF [143], Li_3N [144]) and Li alloys (e.g., Li-Sb [145], Li-Ag [146]) exhibit excellent compatibility and wettability with SSEs. These materials, due to their higher adsorption energy and reduced diffusion barriers, act as fast ion conductors or alloy phases, facilitating rapid Li^+ diffusion at both anode and cathode interfaces and promoting uniform Li deposition during cycling [147]. The in-situ formation of artificial SEI containing relevant lithium salts and Li alloys has been widely investigated to effectively regulate Li deposition/stripping behavior and create more lithium-favorable sites. For example, an ultra-thin and lithiophilic SEI layer of LiF|Li_3Sb was developed on a Li foil through the in-situ transformation of an SbF_3 precursor (Fig. 10**B**), improving even Li deposition and significantly enhancing interface stability [148]. Utilizing the exceptional lithium affinity of $InCl_3$, Leng et al. [140] introduced a SEI formation approach by immersing LLZO flakes in a 50 mM $InCl_3$ isopropanol solution for in-situ reaction (Fig. 10B), which extended the lifespan of symmetric batteries to 4000 h at a current density of 0.2 mA cm^{-2}. Beyond reducing interface impedance and accelerating Li^+ cross-interface transport, gaps/cracks induced by volumetric expansion at the anode interface are filled by uniformly distributed $InLi_x$ nanoparticles. Moreover, SSBs featuring various metal fluorides anode have been documented, where the interface between lithium-free anodes and SSEs is safeguarded through a LiF layer, with metallic Ag acting as an alloying nucleation site to foster uniform Li deposition (Fig. 10**C**) [141]. After depositing lithium of 5 mAh cm^{-2}, a dense composite layer of 24 μm thick was formed, featuring uniformly dispersed Li-Ag alloy and in-situ formed LiF SEI. Once the Li metal is completely removed, Ag and F reconcentrate at the SSEs|Steel Use Stainless (SUS) interface, demonstrating an excellent structural reversibility.

A reliable strategy involves utilizing decomposition products as effective SEI components [149–151]. Traditional injection/spraying techniques, typically aimed at enhancing substrate lithiophilicity and employing soaking in molten Li (SML), struggle to establish a uniform and robust SEI to inhibit side reactions [152,153]. Wang et al. [142] introduced a self-diffusion strategy (RSD) to construct a stable and compact SEI layer, propelled by the surface concentration gradient of liquid Li and fluid dynamics. Unlike the SML approach, which relies on the adsorption affinity of composite anodes for molten Li to absorb liquid Li upwards against gravity (Fig. 10**D**), the RSD method positions substrates (e.g., CuO, Cu_2S, CuF_2) below Li metal and maintains elevated temperatures for several minutes to boost fluid diffusion kinetics, allowing products to uniformly concentrate on the surface of molten Li. Finite element analysis further elucidated the diffusion behavior of interface products (Fig. 10**E**), highlighting the uneven distribution of side reaction products in the SML route due to temperature gradients during molten Li adsorption to lithiophilic substrates, as dictated by Fick's law, preventing their effective migration to the Li surface to form a stable interface. In contrast, the RSD strategy, through uniform temperature-induced thermal convection, provides a migration pathway for molten Li, enabling products to diffuse uniformly to the surface of molten Li and form a consistent SEI layer.

3.2.3. Coating layer

In the quest for next-generation SSBs with higher energy density, nickel-rich NCM cathodes emerge as prime candidates over

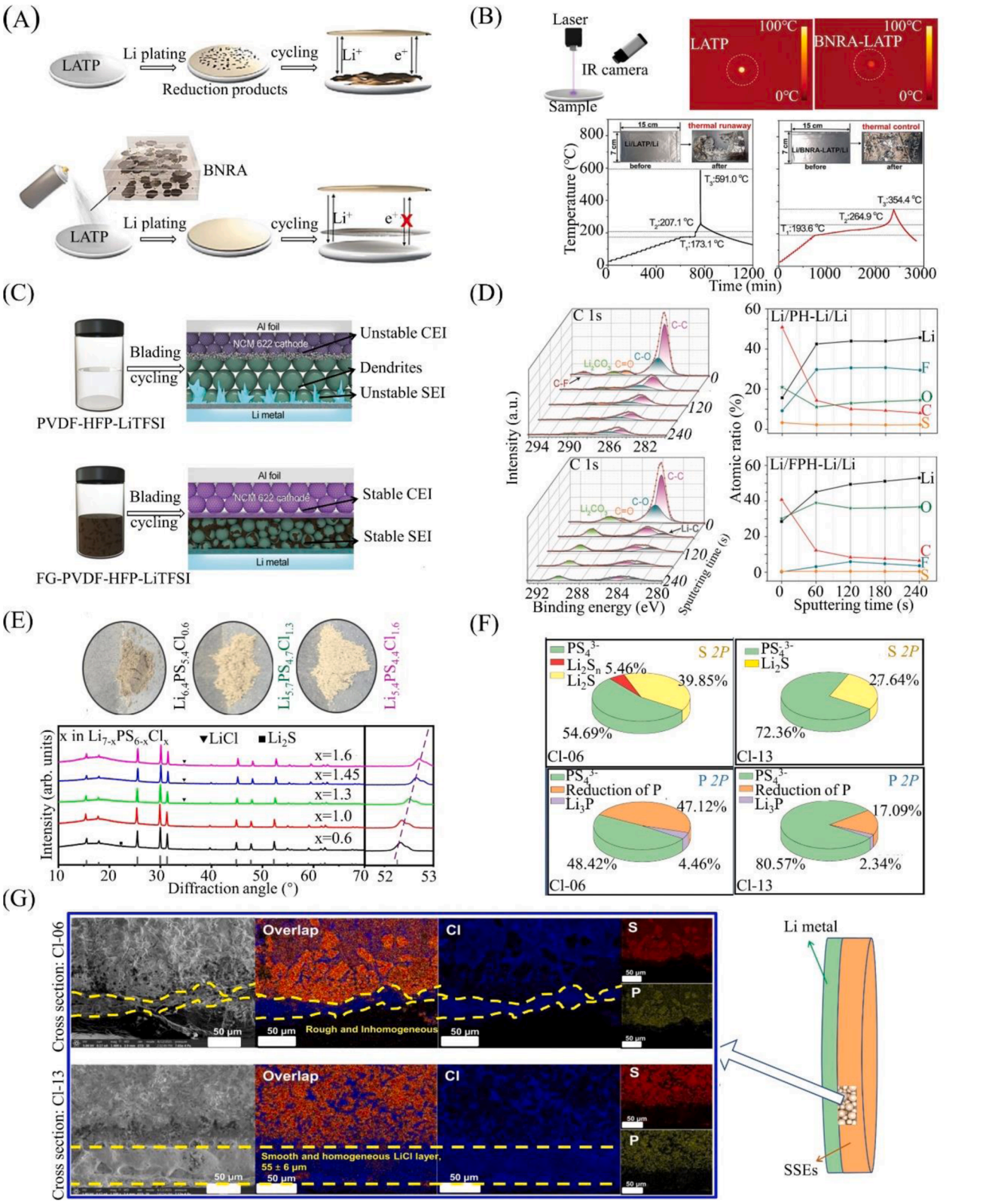

Fig. 9. (A) Schematic of processing LATP pellets with and without BNRA additives. (B) Time-dependent temperature curves of the Li||LATP||Li and Li||BNRA-LATP||Li symmetric cells. The inserts are the appearances of pouch cells before and after ARC tests. [137] Copyright 2022 Wiley-VCH. (C) Schematic of different properties in full cells fabricated with and without fluorinated grapheme. (D) C1s XPS spectrums and corresponding in-depth atomic composition ratios of the cycled Li||PH-Li||Li (above) and Li||FPH-Li||Li (below) symmetric cells. [138] Copyright 2022 Wiley-VCH. (E) XRD patterns of $Li_{7-x}PS_{6-x}Cl_x$ argyrodites. (F) Semi-quantitative analyses of the decomposition at the Li|SSEs interface by XPS analyzing. (G) Cross-section SEM and EDS images for Cl-06 (above) and Cl-13 (below), and an uniform and smooth LiCl layer can be distinguished. [73] Copyright 2022 Springer Nature.

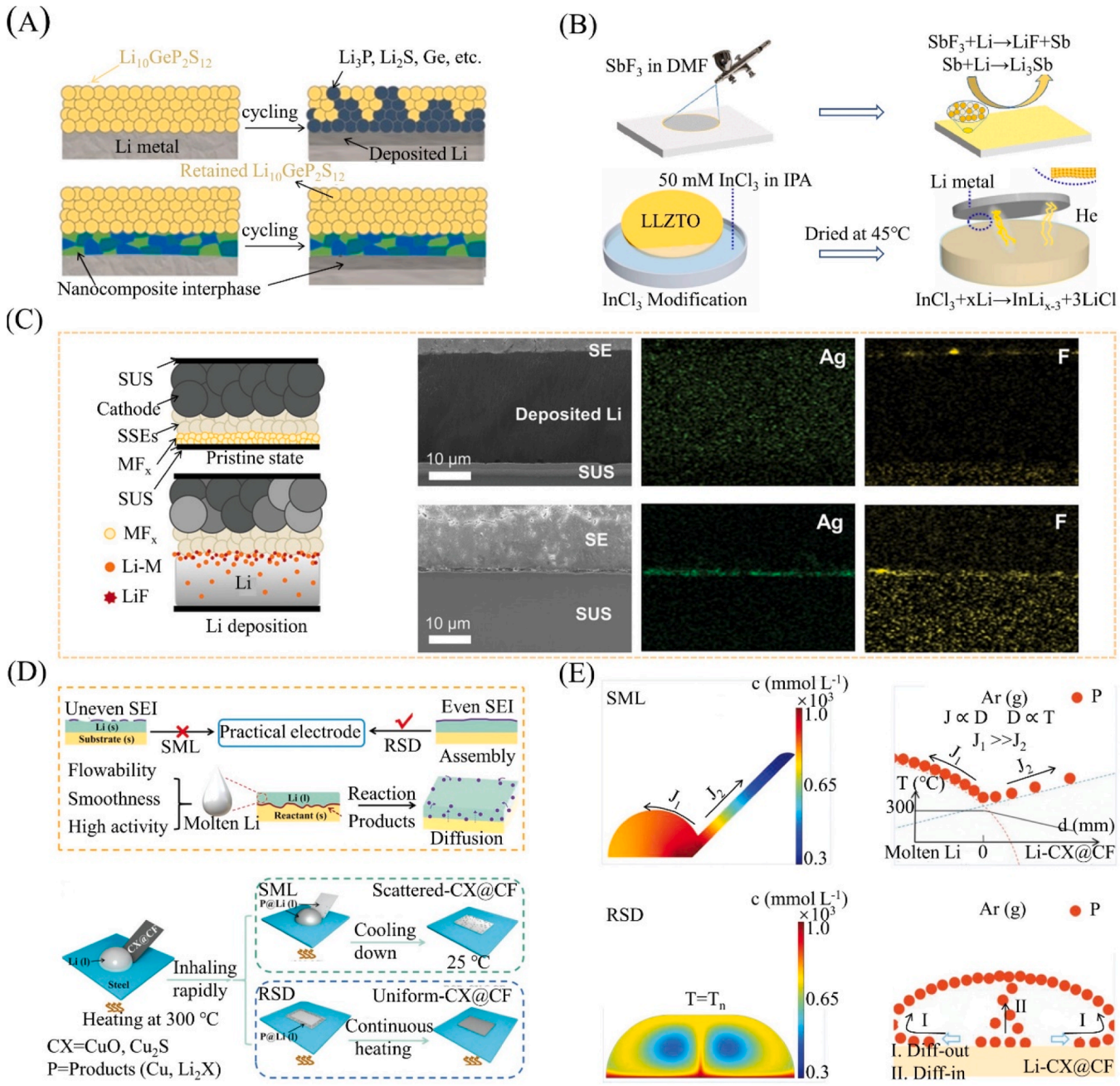

Fig. 10. (A) Schematic of poor interfacial stability (above) and robust interface derived from organic–inorganic nanocomposite SEI (below). [139] Copyright 2018 Wiley-VCH. (B) Schematic of preparations for in-situ converted SEI by spraying and soaking strategies. [140] Copyright 2022 Elsevier. (C) Schematic of Li depositing on MF_x-based electrode (left) and cross-section SEM and EDS images of AgF anode during cycling. [141] Copyright 2022 Wiley-VCH. (D) Conceptions (above) and Different preparation processes (below) for RSD and SML routes. (E) Diffusion behavior of SML (above) and RSD (below) routes analyzed through finite element simulation. [142] Copyright 2022 Wiley-VCH.

conventional LFP cathodes, owing to their superior energy storage capabilities. Nonetheless, the high-voltage operation of these cathodes often triggers severe parasitic reactions at the cathode interface, leading to inevitable capacity degradation and increased impedance, not to mention the oxidation of Ni^{3+} and the accumulation of stress within particles. To mitigate these issues, coating cathode particles with a Li^+ conductive layer has been identified as a promising strategy.

Leveraging advancements in first-principles methodologies and computational technology, the high-throughput computational screening of 104,082 lithium-containing coating compositions has been realized [154]. This screening identified novel poly-anionic oxide coatings (LiH_2PO_4, $LiTi_2(PO_4)_3$, and $LiPO_3$) that exhibit unparalleled phase stability, (electro)chemical stability, and ionic conductivity. Fig. 11**A** highlights the pronounced interactions between all SSEs and cathodes (excluding LLZO and LFP), with deep green and red indicating low and high reactivity, respectively. For instance, the heightened reactivity observed between oxide cathodes and sulfide SSEs primarily stems from the substantial dissociation energy of O-S bonds, significantly surpassing that of P-O and P-S bonds, with minimal differences observed between transition metal-O and transition metal-S bonds, consistent with prior research findings [155,156]. Importantly, garnet-based SSEs are prone to thermodynamic degradation when reacting with oxide cathodes during charging, compromising interface compatibility. A stable interface is thus only attainable when all

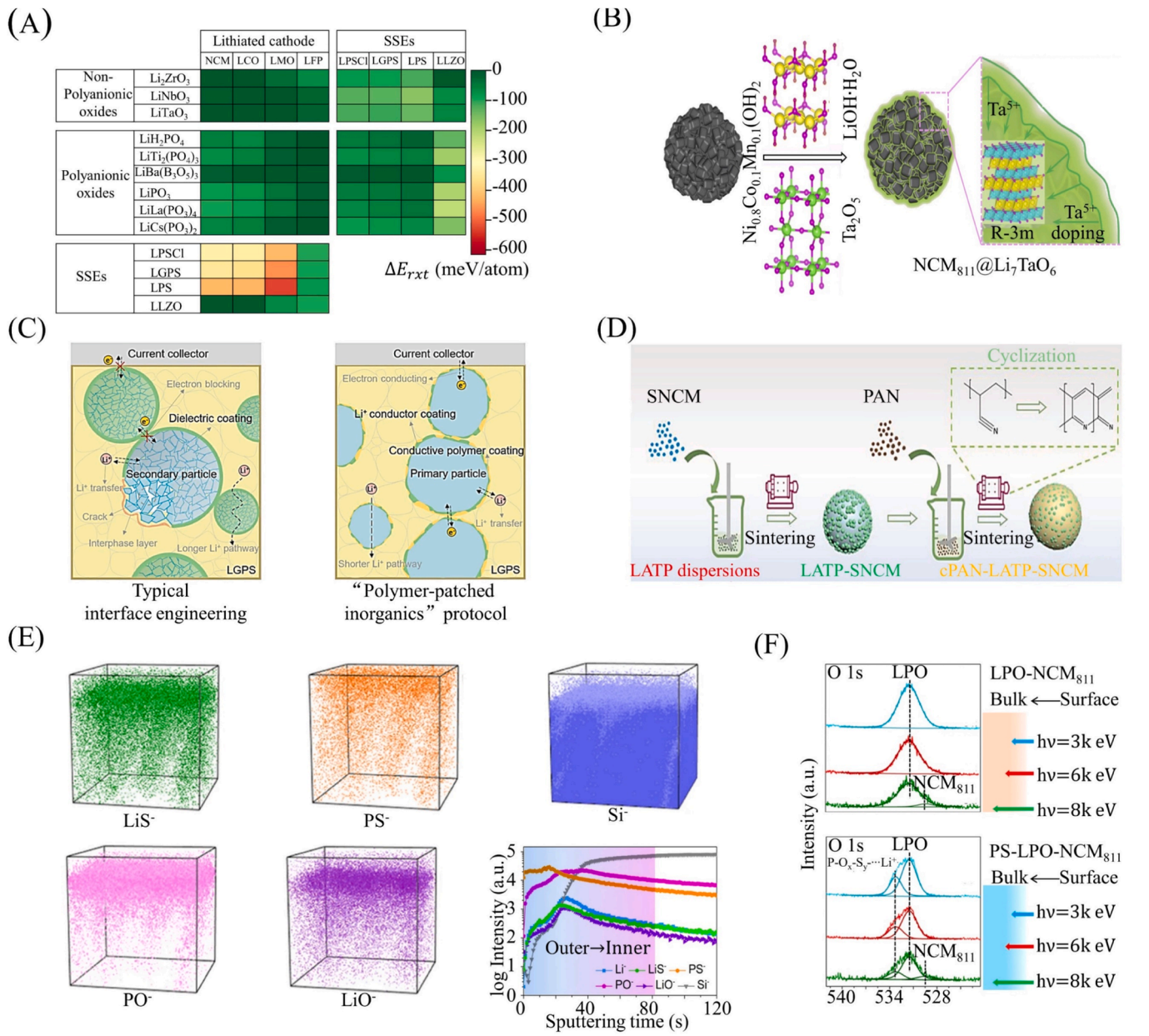

Fig. 11. (A) Reaction energies ΔE_{rxt} of cathode|coating, cathode|SSE and coating|SSE interphases at fully lithiated-state. [154] Copyright 2019 Elsevier. (B) Schematic of preperation for the Li_7TaO_6 coating layers. [157] Copyright 2022 Royal Society of Chemistry. (C) Schematic of facile ion/electron transportations boosted by "polymer-patched inorganic" coating layer. (D) Schematic of preperation for the cPAN-LATP coating layers. [158] Copyright 2022 Wiley-VCH. (E) 3D view images and depth profile of various secondary ion species in PS-LPO-NMC_{811} obtained by TOF-SIMS sputtering. (F) Depth profiles of the LPO-NMC_{811} and the PS-LPO-NMC_{811} samples by HEXPS characterizing. [159] Copyright 2023 Springer Nature.

corresponding cathodes are shielded by alternative coatings.

To experimentally address these interface challenges, a wide array of Li^+ conductor coatings (e.g., $LiNbO_3$ [160], Li_2ZrO_3 [161], $Li_4Ti_5O_{12}$ [162], $LiAlO_2$ [163], Li_3BO_3-Li_2CO_3 [164], etc.) have been adeptly applied, effectively curtailing side reactions at the cathode interface. Shi et al. [157] accomplished simultaneous bulk tantalum doping and surface coating with Li_7TaO_6 (L7TaO) on NCM811 cathodes via a one-step synthesis method (Fig. 11**B**). The nanoscale L7TaO coating and the incorporation of + 5 valence state tantalum not only facilitate Li^+ transfer at the interface but also significantly bolster the reversibility of the *H2→H3* phase transition while suppressing side reactions. Concurrently, SSBs demonstrated exceptional cycling stability at 1 C, achieving 5650 cycles with a mere 0.0069 % capacity fade per cycle.

Despite the advantages of stabilizing interfaces and enhancing Li^+ transport kinetics offered by these Li^+ conductor coatings, they may inadvertently lead to increased polarization due to impeded electron transport (Fig. 11**C**). Liang et al. [158] devised a "polymer-patched inorganic" coating strategy, encapsulating single-crystal NCM622 surfaces (SNCM) with a hybrid coating composed of LATP and cyclized polyacrylonitrile (cPAN). This innovative coating enables the cPAN-LATP-SNCM cathode to withstand high oxidation conditions at elevated potentials while simultaneously enhancing electronic connectivity between SNCM particles and facilitating Li^+ migration at the cathode interface (Fig. 11**D**). Moreover, considering the impact of Li gradient concentration at the interface on Li^+ diffusion during cycling, a novel $Li_3P_{1+x}O_4S_{4x}$ coating was ingeniously designed by partially in-situ sulfidizing Li_3PO_4 on the NCM cathode surface using atomic layer deposition (ALD) [159]. This ensures chemical compatibility with the outermost Li_3PS_4 while averting oxidative decomposition of sulfide SSEs. Experimental findings revealed that the gradient $Li_3P_{1+x}O_4S_{4x}$

coating possesses an oxygen-rich inner surface akin to Li_3PO_4, and a sulfur-rich outer surface, endowed with P-S-…Li^+ and P-O_x-S_y-…Li^+ interactions (Fig. 11**E, F**). This high Li^+ conductive gradient coating markedly elevates the electrochemical performance of the batteries by ensuring minimal interface resistance and swift Li^+ migration.

3.3. Induced-polarization electric field in SCL

Breakthroughs in enhancing Li^+ transport across interfaces have been achieved through strategies such as doping, heterojunction formation, and epitaxial interface growth [165–167]. Among these, introducing dielectric particles, encompassing both paraelectric and ferroelectric types, to redistribute Li concentration via polarization electric fields generated by orderly arranged dipoles (Fig. 12**A**) emerges as a particularly promising approach to modulate the formation of SCL and facilitate Li^+ migration [168,169].

To thoroughly comprehend the mechanism behind the construction of induced electric fields, a ferroelectric mixed amide perchlorate salt, C$(NH_2)_3ClO_4$ (GClO4), synthesized by evaporating an ethanol solution containing perchloric acid and guanidine carbonate, was coated onto the surface of $LiCoO_2$ cathodes (G@LCO) [170]. The flexoelectric effect of G@LCO was elucidated (Fig. 12**B**), effectively mitigating the obstruction posed by SCL to Li^+ transport at the cathode interface and demonstrating satisfactory performance in SSBs under harsh conditions. Additionally, $BaTiO_3$ (BTO) and $SrTiO_3$ (STO) nanoparticles were introduced at the interface for its ferroelectric or paraelectric properties [171]. Thanks to the reversible directionality of dipoles inherent to the ferroelectric properties of BTO/STO, an induced electric field could be readily formed within the SCL, significantly reducing interface impedance. In contrast, ferroelectric nanomaterials with randomly oriented permanent dipoles are nearly ineffective in creating Li^+ transport channels. A high ionic conductivity and dielectric PVDF-based HSEs coupled with BTO and LLTO nanowires (PVBL, ε_r: 8 ~ 12) [175] not only facilitates the dissociation of Li salts (Fig. 12**C**) but also weakens the SCL to some extent, ensuring rapid Li^+ transport at the interface (Fig. 12**D**). Experimental results indicate that the internal electric field, generated by the separation of positive and negative charges to the poles, is advantageous for Li^+ accumulation on BTO. Furthermore, a uniform distribution of electric potential further corroborates that PVBL indeed diminishes the SCL at the cathode interface (Fig. 12**E**).

Beyond the incorporation of dielectric particles, interface modification through tailored carrier concentration and band alignment [173] can also effectively regulate SCL. For example, generating an interface energy barrier by nano-scale thermal deposition of titanium selectively permits Li^+ migration to LLTO while inhibiting electron flow. Specifically, the interlayer titanium, with a higher Fermi level, restricts electron migration to LATP through the regulated SCL, thereby endowing SSBs with enhanced electrochemical stability (Fig. 12**F**). Hence, the above strategies promise to guide the development of practical SSBs by modulating SCL.

Interestingly, piezoelectric materials with asymmetric structures can also generate polarization electric fields, such as $LiTaO_3$ (LTO, with a piezoelectric coefficient of 14.6 pC N^{-1}, and ionic conductivity of 10^{-6}~10^{-5} cm^2 s^{-1}), and its influence on interfacial Li^+ diffusion has not been clarified in the previous studies [176,177]. Dai et al. [174] thus provided novel insights into the Li^+ dynamics and structural stability of $Li[Ni_xCo_yMn_{1-x-y}]O_2$ (x = 0.6, 0.8) cathode interfaces coated with LTO (Fig. 12**G**). In a highly lithiated state, the additional polarization electric field, aligned with the external electric field, promotes rapid Li^+ transport, benefiting from alleviated lattice degradation. Moreover, the LTO coating layer, acting as a dynamic volume-changing physical barrier, also mitigates stress-strain accumulation. This synergy of mechanical and electric field effects with piezoelectric materials could potentially advance the application of SSBs.

4. Summary and perspectives

SSBs have emerged as a transformative solution in energy storage, heralded for their non-leakage properties, flame resistance, and high mechanical strength. These characteristics significantly reduce operational safety risks, aligning with the growing demand for higher energy densities. Nonetheless, challenges such as dendritic lithium growth during cycling, excessive polarization, and rapid capacity fade hinder the path to their widespread adoption. Achieving efficient Li^+ transport across interfaces is pivotal for high-performance SSBs, with a crucial focus on enhancing the understanding and design of Li^+ interface transport dynamics. The scientific community is vigorously pursuing solutions to these obstacles, focusing on electrolyte material advancements, protective coatings, and novel electrode-electrolyte configurations to accelerate the commercialization of SSBs.

To address the SSEs|electrode interface issues, numerous studies have shed light on the mechanisms behind these phenomena. Issues like void creation, formation of undesired decomposition products, and SCL stem from lithium flux imbalance, thermodynamic instability, and disparities in electrode electrochemical potentials, which hinder Li^+ migration at the interface. Advanced characterizations, including HAADF-STEM, TOF-SIMS, HEXPS, MAS NMR, in-situ Raman, XANES spectroscopy, and in-situ EIS, have been employed to study Li^+ transport behavior at the interface and the associated chemical environments. Strategies such as interface wettability enhancement, side reaction mitigation, and introduction of polarization electric fields have been suggested to elevate the electrochemical performance of SSBs. The refinement of electrode interface impedance and D_{Li^+} significantly mirrors the bolstered kinetics of Li^+ traversal across interfaces (Table 1).

Despite significant progress in designing stable interfaces for rapid Li^+ transport, SSBs face critical challenges, including improving SSEs| electrode contact, minimizing side reactions, and optimizing the SCL to enhance performance.

I. The SSEs|electrode interface is crucial for efficient Li^+ transport. Poor interface contact increases resistance, decreased ionic conductivity, and diminished battery performance. Interface engineering strategies, such as modifying electrode or SSEs surfaces to form lithiophilic conductive interfaces, are essential (Fig. 13**A**) [181]. Approaches like in-situ solidification enhance contact by filling gaps, though issues like potential cracking and limited thermal stability remain. Buffer layers alleviate mechanical stress and suppress dendrite growth but add manufacturing complexity. Combining with polymers or additives, HSEs improve flexibility and fill interface irregularities, boosting ionic conductivity. Additionally, IL lower interface impedance and improve wettability but may introduce side reactions and incur higher costs. While applying external pressure can improve contact, precise control is required to avoid damaging components. Accelerating material screening through machine learning and developing databases of fast Li^+ conductors can further optimize electrolyte performance **(**Fig. 13**B, E)**.

II. Side reactions at the SSEs|electrode interface undermine battery stability and safety. Developing advanced materials to form uniform, stable and ion-conductive SEI/CEI is crucial to protecting Li metal anodes and high-capacity cathodes. Artificial SEI layers reduce dendrite growth and optimize Li^+ transport but often involve complex preparation. Similarly, coating layers enhance chemical stability and prevent adverse reactions but face adhesion and cost challenges. Engineering fast Li^+ conducting SSEs through structural and compositional modifications offers a practical pathway to mitigate these issues and enhance compatibility with electrode materials (Fig. 13**C, E**).

III. The SCL plays a significant role in ion transport at the SSEs| electrode interface. Its properties can be optimized using SCL modifications, including dielectric, piezoelectric, and band structure tuning. Dielectric adjustments enhance interfacial electric fields, piezoelectric effects alleviate mechanical stress, and band structure engineering suppresses side reactions while promoting favorable charge distribution.

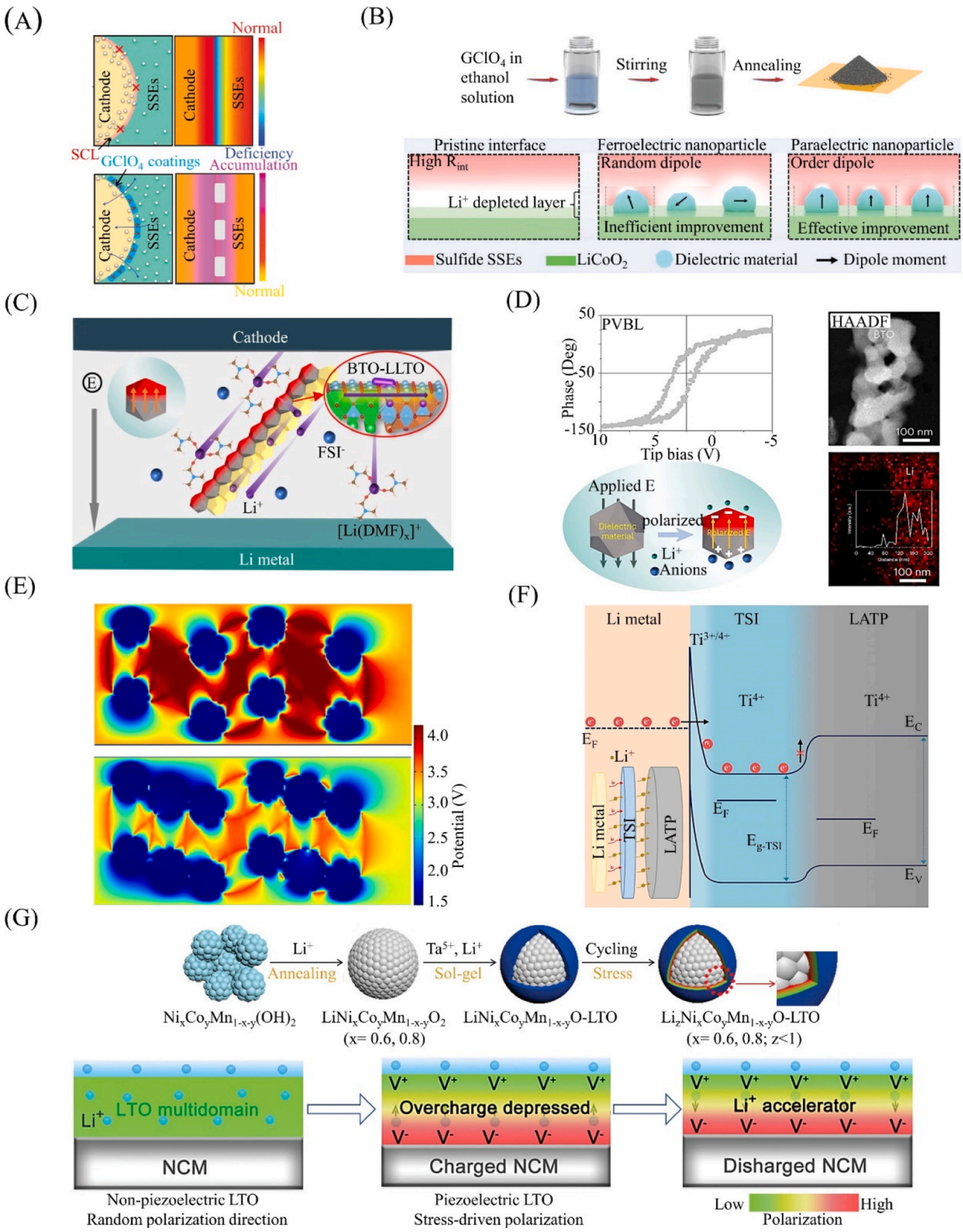

Fig. 12. (A) Schematic of the typical SCL (above) and regulated SCL by ferroelectric $GClO_4$ doping (below). [170] Copyright 2023 Wiley-VCH. (B) Fabricating process of $GClO_4$-coated $LiCoO_2$ cathode (above) and different environments at the interface derived by ferroelectric and paraelectric particles (below). [171] Copyright 2022 Wiley-VCH. (C) Schematic of the Li salt dissociation and Li^+ transportation along the PVBL SSEs. (D) Hysteresis loop, HAADF-STEM image, corresponding EELS of Li element and polarized potential of the PVBL SSEs, clockwise. (E) COMSOL simulations of the potential distribution in SSEs without (above) and with BTO-LLTO nanowires (below). [172] Copyright 2023 Springer Nature. (F) Energy band diagram at the interface for the Li||Ti@LATP@Ti||Li symmetrical cell during charging. [173] Copyright 2021 Wiley-VCH. (G) Schematic of the preparation of LTO-coated cathode (above) and the polarization and regulating effects of LTO on interfacial Li^+ diffusion. [174] Copyright 2022 Wiley-VCH.

Table 1
Kinetic designs and corresponding electrochemical performance at room temperature. (Where the Promotion of R_{int} were calculated by $-\Delta R_{int}/R_{blank\ group}$ for symmetric cells).

Constitution of symmetric cells and full cells	Promotion of R_{int}	σ_{Li^+} (or D_{Li^+})	Cycling performances of symmetric cells	Cycling performances of full cells	Method	Ref.
Li||DLC||Li, Li ||DLC||LFP	96.67 %	1.70×10^{-4} S cm^{-1}	450 h under 0.3 mA cm^{-2} and 0.15 mAh cm^{-2}	122.0 mAh g^{-1} at 0.5 C after 130 cycles	In situ solidification	[91]
Li||UV-SPEs||Li, Li||UV-SPEs||aligned-LFP	94.22 %	1.80×10^{-4} S cm^{-1}	1000 h under 0.05 mA cm^{-2} and 0.05 mAh cm^{-2}	142.0 mAh g^{-1} at 0.1 C after 120 cycles	In situ solidification	[94]
Li||$Al(OTf)_3$||Li, Li||$Al(OTf)_3$|| CNTs@LFP@PDL	98.71 %	2.50×10^{-11} cm^2 s^{-1}	2400 h	132.2 mAh g^{-1} at 0.5 C after 200 cycles	In situ solidification	[178]
Li||LPSCl-P(PEGMEA) ||Li, Li||LPSCl-P(PEGMEA) || NCM_{811}	84.20 % (60 °C for 36 h)	4.60×10^{-4} S cm^{-1}	500 h under 0.25 mA cm^{-2} and 0.25 mAh cm^{-2}	128.0 mAh g^{-1} at 0.1 C after 90 cycles	In situ solidification	[179]
Li||LNO10-LLZTO- LNO10|| Li, Li||LNO10-LLZTO||LFP	99.67 %	2.36×10^{-10} cm^2 s^{-1}	4500 h under 0.3 mA cm^{-2} and 0.15 mAh cm^{-2}	118.8 mAh g^{-1} at 1 C after 500 cycles	In situ solidification	[101]
Li||LSCE||Li, Li||LSCE||NCM_{622}	~99.95 %	1.25×10^{-4} S cm^{-1}	1600 h under 0.1 mA cm^{-2} and 0.2 mAh cm^{-2}	106.9 mAh g^{-1} at 0.5 C after 200 cycles	Buffer layer	[108]
$Li_{0.8}Al$||LGPS||$Li_{0.8}Al$, $Li_{0.8}Al$||LGPS||S	77.69 %	/	2500 h under 0.5 mA cm^{-2} and 0.5 mAh cm^{-2}	1237.0 mAh g^{-1} at 0.2 C after 200 cycles	Buffer layer	[180]
Li||AIOC||Li, Li||AIOC||LFP	86.49 %	2.21×10^{-5} S cm^{-1}	100 h under 0.1 mA cm^{-2} and 0.2 mAh cm^{-2}	103.8 mAh g^{-1} at 0.5 C after 100 cycles	Buffer layer	[112]
Li||Al-LAGP-Al||Li, Li||Al-LAGP-Al||LFP	82.28 %	2.50×10^{-4} S cm^{-1}	1000 h under 0.1 mA cm^{-2} and 0.1 mAh cm^{-2}	130.0 mAh g^{-1} at 0.1 C after 160 cycles	Buffer layer	[111]
Li||IL@SPF-LATP||Li, Li||IL@SPF-LATP||LFP	61.82 %	/	1000 h under 0.1 mA cm^{-2} and 0.1 mAh cm^{-2}	130.0 mAh g^{-1} at 0.1 C after 160 cycles	Buffer layer	[110]
Li||$P_{12}LP=$ |Li, Li||$P_{12}LP=$ |LFP	~86.67 %	1.07×10^{-4} S cm^{-1}	650 h under 0.05 mA cm^{-2} and 0.05 mAh cm^{-2}	120.0 mAh g^{-1} at 0.1 C after 100 cycles	Ionic liquid	[41]
Li||PTLI-LLZTO-PTLI||Li, Li||PTLI-LLZTO-PTLI||LFP	99.51 %	2.89×10^{-4} S cm^{-1}	1000 h under 0.05 mA cm^{-2} and 0.003 mAh cm^{-2}	144.8 mAh g^{-1} at 0.2 C after 100 cycles	Ionic liquid	[13]
Li||40PIL-IL-GF= |Li, Li||40PIL-IL-GF= |NCM_{811}	/	0.80×10^{-3} S cm^{-1}	1700 h under 0.1 mA cm^{-2} and 1 mAh cm^{-2}	162.0 mAh g^{-1} at 0.1 mA cm^{-2} after 600 cycles	Ionic liquid	[131]
Li||BNRA-LATP||Li, Li||BNRA-LATP||LFP	~70.00 % (Standing for 48 h)	1.69×10^{-4} S cm^{-1}	1800 h under 0.05 mA cm^{-2} and 0.025 mAh cm^{-2}	~140.0 mAh g^{-1} at 0.5 C after 500 cycles	SSEs modification	[137]
Li||FPH-Li||Li, Li||FPH-Li||NCM_{622}	~79.68 %	1.32×10^{-4} S cm^{-1} at 30 ℃	900 h under 0.1 mA cm^{-2} and 0.1 mAh cm^{-2} at 30 ℃	~100.0 mAh g^{-1} at 1 C after 300 cycles	SSEs modification	[138]
Li||$Li_{5.7}PS_{4.7}Cl_{1.3}$||Li, Li||$Li_{5.7}PS_{4.7}Cl_{1.3}$|| LNO@NCM_{622}	~94.66 % (Standing for 600 h)	5.30×10^{-3} S cm^{-1}	1000 h under 0.5 mA cm^{-2} and 0.25 mAh cm^{-2}	137.0 mAh g^{-1} at 0.1 mA cm^{-2} after 30 cycles	SSEs modification	[73]
Li||PEO-LiTFSI-Li_2S||Li, Li||PEO-LiTFSI-Li_2S|| NCM_{811}	74.29 %	/	1800 h under 0.1 mA cm^{-2} and 0.1 mAh cm^{-2} at 50 ℃	139.0 mAh g^{-1} at 0.2 mA cm^{-2} after 150 cycles	Artificial SEI	[144]
SbF_3@Li||PEO-LLZTO|| SbF_3@Li, SbF_3@Li||PEO-LLZTO|| LFP	/	/	320 h under 0.2 mA cm^{-2} and 0.2 mAh cm^{-2} at 50 ℃	150.0 mAh g^{-1} at 0.2 C after 200 cycles	Artificial SEI	[148]
Li||TCF-garnet||Li, Li||TCF-garnet||S	99.02 %	4.40×10^{-4} S cm^{-1}	690 h under 0.3 mA cm^{-2} and 0.15 mAh cm^{-2}	775.0 mAh g^{-1} at 0.5 C after 1000 cycles	Artificial SEI	[142]
Li||LPS||NCA@LZO	83.65 % (after 100 cycles)	/	/	80 % capacity retention at 0.1 C after 100 cycles	Coating layer	[161]
Li||LPSCl|| NCM_{701515}@LTO2	~80.00 %	/	/	64.8 mAh g^{-1} at 0.25 C after 100 cycles	Coating layer	[162]
LiIn ||LPSCl|| NCM_{811}@L7TaO	51.95 % (after 200 cycles)	~1.00×10^{-12} cm^2 s^{-1} for coating layer	/	80.2 mAh g^{-1} at 1 C after 5650 cycles	Coating layer	[157]
LiIn||LPSCl||$GClO_4$@LCO		7.90×10^{-10} cm^2 s^{-1} for coating layer	/	100.0 mAh g^{-1} at 0.5 C and 30 ℃ after 200 cycles	Induced-polarization electric field	[170]
LiIn||LPSCl||LCO@STO-C	66.58 %	/	/	137.9 mAh g^{-1} at 0.1 C after 50 cycles	Induced-polarization electric field	[171]
Li||PVBL||Li, Li||PVBL||NCM_{811}	71.25 % (Full cells at −20 ℃)	8.20×10^{-4} S cm^{-1}	1900 h under 0.1 mA cm^{-2} and 0.1 mAh cm^{-2}	121.0 mAh g^{-1} at 1 C after 1000 cycles	Induced-polarization electric field	[175]

These strategies lower Li^+ migration barriers and improve stability, but their complex fabrication and potential electron leakage pose challenges. Furthermore, advanced characterization techniques can further clarify SCL formation mechanisms and guide better interface designs (Fig. 13**D, E**).

In summary, advancing the development of SSBs requires a multifaceted approach addressing SSEs|electrode interface challenges, minimizing side reactions, and leveraging the properties of the SCL. A balanced approach leveraging innovative materials and design strategies can yield SSBs with higher energy densities, longer cycle lives, and improved safety, paving the way for widespread application in next-generation energy storage systems (Fig. 13**F**).

CRediT authorship contribution statement

Shao Guangjie: Writing – review & editing, Supervision. **Liu Ming:**

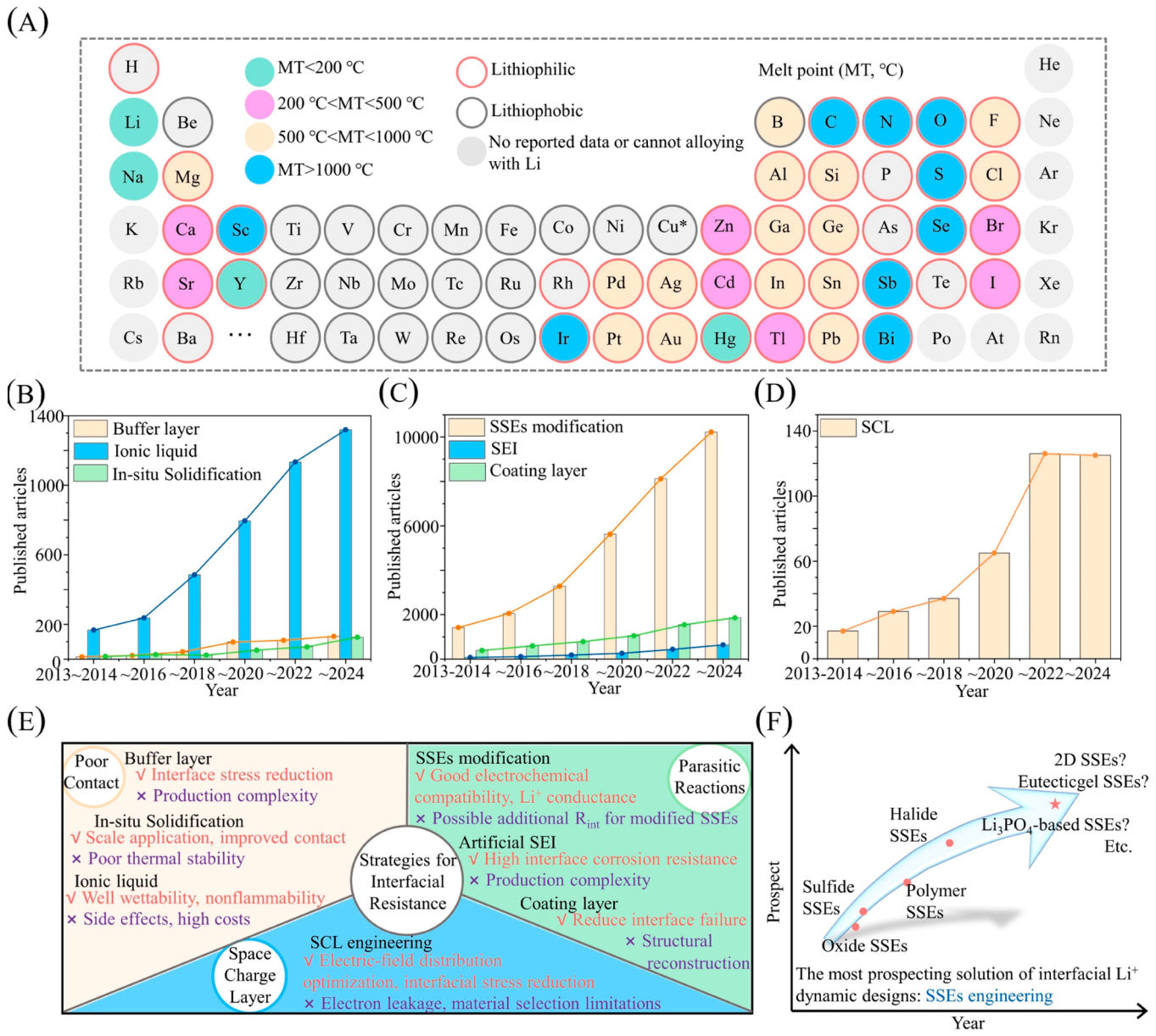

Fig. 13. (A) Periodic table of the lithiophilic elements and corresponding melt point. (*: Cu and Li can form alloy at 270 ℃ [172].) (B~D) Publication trends in SSBs for poor contact, parasitic reactions and SCL. (E) Comparison of the advantages and disadvantages of strategies related to enhancing interfacial Li^+ dynamics. (F) Prospect of the interfacial Li^+ transfer designs: SSEs engineering.

Writing – original draft, Investigation. **Wang Guoxiu:** Writing – review & editing. **Tian Hao:** Writing – review & editing, Supervision, Conceptualization. **Ma Zhipeng:** Writing – review & editing, Supervision, Investigation, Funding acquisition, Conceptualization. **Song Ailing:** Writing – review & editing, Methodology, Investigation, Funding acquisition. **Zhang Xinyi:** Writing – original draft, Investigation. **Wang Jie:** Writing – original draft, Investigation. **Fan Yuqian:** Investigation.

Declaration of Competing Interest

The authors declare that they have no known competing financial interests or personal relationships that could have appeared to influence the work reported in this paper.

Acknowledgements

This work was financially supported by the National Natural Science Foundation of China (52174281 and 52074241), the Natural Science Foundation of Hebei Province (E2023203209 and B2021203016), the Hebei Provincial Department of Human Resources and Social Security (C20230328), the Subsidy for Hebei Key Laboratory of Applied Chemistry after Operation Performance (22567616H).

Data availability

Data will be made available on request.

References

[1] K. Brandt, Historical development of secondary lithium batteries, Solid State Ion.-. 69 (1994) 173–183, https://doi.org/10.1016/0167-2738(94)90408-1.
[2] E. Fan, L. Li, Z. Wang, J. Lin, Y. Huang, Y. Yao, R. Chen, F. Wu, Sustainable recycling technology for Li-ion batteries and beyond: challenges and future prospects, Chem. Rev. 120 (2020) 7020–7063, https://doi.org/10.1021/acs.chemrev.9b00535.

[3] J.B. Goodenough, Y. Kim, Challenges for rechargeable Li batteries, Chem. Mater. 22 (2010) 587–603, https://doi.org/10.1021/cm901452z.

[4] Y.S. Jung, D.Y. Oh, Y.J. Nam, K.H. Park, Issues and challenges for bulk-type all-solid-state rechargeable lithium batteries using sulfide solid electrolytes, Isr. J. Chem. 55 (2015) 472–485, https://doi.org/10.1002/ijch.201400112.

[5] Z. Li, R. Yu, S. Weng, Q. Zhang, X. Wang, X. Guo, Tailoring polymer electrolyte ionic conductivity for production of low- temperature operating quasi-all-solid-state lithium metal batteries, Nat. Commun. 14 (2023) 482, https://doi.org/10.1038/s41467-023-35857-x.

[6] H. Liu, X.-B. Cheng, J.-Q. Huang, H. Yuan, Y. Lu, C. Yan, G.-L. Zhu, R. Xu, C.-Z. Zhao, L.-P. Hou, C. He, S. Kaskel, Q. Zhang, Controlling dendrite growth in solid-state electrolytes, ACS Energy Lett. 5 (2020) 833–843, https://doi.org/10.1021/acsenergylett.9b02660.

[7] K. Liu, Y. Liu, D. Lin, A. Pei, Y. Cui, Materials for lithium-ion battery safety, Sci. Adv. 4 (2018) eaas9820, https://doi.org/10.1126/sciadv.aas9820.

[8] V. Raj, V. Venturi, V.R. Kankanallu, B. Kuiri, V. Viswanathan, N.P.B. Aetukuri, Direct correlation between void formation and lithium dendrite growth in solid-state electrolytes with interlayers, Nat. Mater. 21 (2022) 1050–1056, https://doi.org/10.1038/s41563-022-01264-8.

[9] V. Reisecker, F. Flatscher, L. Porz, C. Fincher, J. Todt, I. Hanghofer, V. Hennige, M. Linares-Moreau, P. Falcaro, S. Ganschow, S. Wenner, Y.M. Chiang, J. Keckes, J. Fleig, D. Rettenwander, Effect of pulse-current-based protocols on the lithium dendrite formation and evolution in all-solid-state batteries, Nat. Commun. 14 (2023) 2432, https://doi.org/10.1038/s41467-023-37476-y.

[10] J.M. Tarascon, M. Armand, Issues and challenges facing rechargeable lithium batteries, Nature 414 (2001) 359–367, https://doi.org/10.1038/35104644.

[11] D. Wang, L.-J. Jhang, R. Kou, M. Liao, S. Zheng, H. Jiang, P. Shi, G.-X. Li, K. Meng, D. Wang, Realizing high-capacity all-solid-state lithium-sulfur batteries using a low-density inorganic solid-state electrolyte, Nat. Commun. 14 (2023) 1895, https://doi.org/10.1038/s41467-023-37564-z.

[12] M.S. Whittingham, Lithium batteries and cathode materials, Chem. Rev. 104 (2004) 4271–4302, https://doi.org/10.1021/cr020731c.

[13] Y.-C. Yin, J.-T. Yang, J.-D. Luo, G.-X. Lu, Z. Huang, J.-P. Wang, P. Li, F. Li, Y.-C. Wu, T. Tian, Y.-F. Meng, H.-S. Mo, Y.-H. Song, J.-N. Yang, L.-Z. Feng, T. Ma, W. Wen, K. Gong, L.-J. Wang, H.-X. Ju, Y. Xiao, Z. Li, X. Tao, H.-B. Yao, A $LaCl_3$-based lithium superionic conductor compatible with lithium metal, Nature 616 (2023) 77–83, https://doi.org/10.1038/s41586-023-05899-8.

[14] Y. Zhao, Z. Chen, F. Mo, D. Wang, Y. Guo, Z. Liu, X. Li, Q. Li, G. Liang, C. Zhi, Aqueous rechargeable metal-ion batteries working at subzero temperatures, Adv. Sci. 8 (2021) 2002590, https://doi.org/10.1002/advs.202002590.

[15] H. Wan, Z. Wang, S. Liu, B. Zhang, X. He, W. Zhang, C. Wang, Critical interphase overpotential as a lithium dendrite-suppression criterion for all-solid-state lithium battery design, Nat. Energy 8 (2023) 473–481, https://doi.org/10.1038/s41560-023-01231-w.

[16] J. Chen, C. Zhao, D. Xue, L. Zhang, T. Yang, C. Du, X. Zhang, R. Fang, B. Guo, H. Ye, H. Li, Q. Dai, J. Zhao, Y. Li, S.J. Harris, Y. Tang, F. Ding, S. Zhang, J. Huang, Lithium deposition-induced fracture of carbon nanotubes and its implication to solid-state batteries, Nano Lett. 21 (2021) 6859–6866, https://doi.org/10.1021/acs.nanolett.1c01910.

[17] C. Lee, S.Y. Han, J.A. Lewis, P.P. Shetty, D. Yeh, Y. Liu, E. Klein, H.-W. Lee, M. T. McDowell, Stack pressure measurements to probe the evolution of the lithium–solid-state electrolyte interface, ACS Energy Lett. 6 (2021) 3261–3269, https://doi.org/10.1021/acsenergylett.1c01395.

[18] A. Ramasubramanian, V. Yurkiv, T. Foroozan, M. Ragone, R. Shahbazian-Yassar, F. Mashayek, Lithium diffusion mechanism through solid–electrolyte interphase in rechargeable lithium batteries, J. Phys. Chem. C. 123 (2019) 10237–10245, https://doi.org/10.1021/acs.jpcc.9b00436.

[19] Y. Tang, L. Zhang, J. Chen, H. Sun, T. Yang, Q. Liu, Q. Huang, T. Zhu, J. Huang, Electro-chemo-mechanics of lithium in solid state lithium metal batteries, Energy Environ. Sci. 14 (2021) 602–642, https://doi.org/10.1039/D0EE02525A.

[20] L. Zhang, T. Yang, C. Du, Q. Liu, Y. Tang, J. Zhao, B. Wang, T. Chen, Y. Sun, P. Jia, H. Li, L. Geng, J. Chen, H. Ye, Z. Wang, Y. Li, H. Sun, X. Li, Q. Dai, Y. Tang, Q. Peng, T. Shen, S. Zhang, T. Zhu, J. Huang, Lithium whisker growth and stress generation in an In Situ atomic force microscope–environmental transmission electron microscope set-up, Nat. Nanotechnol. 15 (2020) 94–98, https://doi.org/10.1038/s41565-019-0604-x.

[21] S. Jeong, Y. Li, W.H. Sim, J. Mun, J.K. Kim, H.M. Jeong, Advances of sulfide-type solid-state batteries with negative electrodes: progress and perspectives, EcoMat 5 (2023) e12338, https://doi.org/10.1002/eom2.12338.

[22] P. Oh, J. Yun, J.H. Choi, K.S. Saqib, T.J. Embleton, S. Park, C. Lee, J. Ali, K. Ko, J. Cho, Development of high-energy anodes for all-solid-state lithium batteries based on sulfide electrolytes, Angew. Chem., Int. Ed. 61 (2022) e202201249, https://doi.org/10.1002/anie.202201249.

[23] B. Li, Z. Sun, N. Lv, Y. Hu, L. Jiang, Z. Zhang, F. Liu, Dual protection of a Li–Ag alloy anode for all-solid-state lithium metal batteries with the argyrodite Li_6PS_5Cl solid electrolyte, ACS Appl. Mater. Interfaces 14 (2022) 37738–37746, https://doi.org/10.1021/acsami.2c09013.

[24] Y. Liang, C. Shen, H. Liu, C. Wang, D. Li, X. Zhao, L.-Z. Fan, Tailoring conversion-reaction-induced alloy interlayer for dendrite-free sulfide-based all-solid-state lithium-metal battery, Adv. Sci. 10 (2023) 2300985, https://doi.org/10.1002/advs.202300985.

[25] C. Yang, H. Xie, W. Ping, K. Fu, B. Liu, J. Rao, J. Dai, C. Wang, G. Pastel, L. Hu, An electron/ion dual-conductive alloy framework for high-rate and high-capacity solid-state lithium-metal batteries, Adv. Mater. 31 (2019) 1804815, https://doi.org/10.1002/adma.201804815.

[26] H. Li, L. Li, J. Zheng, H. Huang, H. Zhang, B. An, X. Geng, C. Sun, Thermal DEcomposition Assisted Construction of Nano-Li_3N sites interface layer enabling homogeneous Li deposition, ChemSusChem 16 (2023) e202202220, https://doi.org/10.1002/cssc.202202220.

[27] L. Ye, X. Li, A dynamic stability design strategy for lithium metal solid state batteries, Nature 593 (2021) 218–222, https://doi.org/10.1038/s41586-021-03486-3.

[28] Y. Lu, C.-Z. Zhao, R. Zhang, H. Yuan, L.-P. Hou, Z.-H. Fu, X. Chen, J.-Q. Huang, Q. Zhang, The carrier transition from Li atoms to Li vacancies in solid-state lithium alloy anodes, Sci. Adv. 7 (2021) eabi5520, https://doi.org/10.1126/sciadv.abi5520.

[29] Z. Deng, S. Chen, K. Yang, Y. Song, S. Xue, X. Yao, L. Yang, F. Pan, Tailoring interfacial structures to regulate carrier transport in solid-state batteries, Adv. Mater. 36 (2024) 2407923, https://doi.org/10.1002/adma.202407923.

[30] X. Chen, X. Li, L. Luo, S. He, J. Chen, Y. Liu, H. Pan, Y. Song, R. Hu, Practical application of all-solid-state lithium batteries based on high-voltage cathodes: challenges and progress, Adv. Energy Mater. 13 (2023) 2301230, https://doi.org/10.1002/aenm.202301230.

[31] S. Dong, L. Sheng, L. Wang, J. Liang, H. Zhang, Z. Chen, H. Xu, X. He, Challenges and prospects of all-solid-state electrodes for solid-state lithium batteries, Adv. Funct. Mater. 33 (2023) 2304371, https://doi.org/10.1002/adfm.202304371.

[32] L. Han, L. Wang, Z. Chen, Y. Kan, Y. Hu, H. Zhang, X. He, Incombustible polymer electrolyte boosting safety of solid-state lithium batteries: a review, Adv. Funct. Mater. 33 (2023) 2300892, https://doi.org/10.1002/adfm.202300892.

[33] B. Qi, X. Hong, Y. Jiang, J. Shi, M. Zhang, W. Yan, C. Lai, A review on engineering design for enhancing interfacial contact in solid-state lithium–sulfur batteries, Nano-Micro Lett. 16 (2024) 71, https://doi.org/10.1007/s40820-023-01306-z.

[34] C. Wang, K. Fu, S.P. Kammampata, D.W. McOwen, A.J. Samson, L. Zhang, G. T. Hitz, A.M. Nolan, E.D. Wachsman, Y. Mo, V. Thangadurai, L. Hu, Garnet-Type Solid-State Electrolytes: Materials, Interfaces, and Batteries, Chem. Rev. 120 (2020) 4257–4300, https://doi.org/10.1021/acs.chemrev.9b00427.

[35] W. Xia, Y. Zhao, F. Zhao, K. Adair, R. Zhao, S. Li, R. Zou, Y. Zhao, X. Sun, Antiperovskite Electrolytes for Solid-State Batteries, Chem. Rev. 122 (2022) 3763–3819, https://doi.org/10.1021/acs.chemrev.1c00594.

[36] Z. Jian, Y.-S. Hu, X. Ji, W. Chen, NASICON-Structured Materials for Energy Storage, Adv. Mater. 29 (2017) 1601925, https://doi.org/10.1002/adma.201601925.

[37] D. Wang, G. Zhong, W.K. Pang, Z. Guo, Y. Li, M.J. McDonald, R. Fu, J.-X. Mi, Y. Yang, Toward Understanding the Lithium Transport Mechanism in Garnet-type Solid Electrolytes: Li^+ Ion Exchanges and Their Mobility at Octahedral/Tetrahedral Sites, Chem. Mater. 27 (2015) 6650–6659, https://doi.org/10.1021/acs.chemmater.5b02429.

[38] T. Asano, A. Sakai, S. Ouchi, M. Sakaida, A. Miyazaki, S. Hasegawa, Solid Halide Electrolytes with High Lithium-Ion Conductivity for Application in 4 V Class Bulk-Type All-Solid-State Batteries, Adv. Mater. 30 (2018) 1803075, https://doi.org/10.1002/adma.201803075.

[39] X. Li, J.T. Kim, J. Luo, C. Zhao, Y. Xu, T. Mei, R. Li, J. Liang, X. Sun, Structural Regulation of Halide Superionic Conductors for All-Solid-State Lithium Batteries, Nat. Commun. 15 (2024) 53, https://doi.org/10.1038/s41467-023-43886-9.

[40] X. Li, J. Liang, N. Chen, J. Luo, K.R. Adair, C. Wang, M.N. Banis, T.-K. Sham, L. Zhang, S. Zhao, S. Lu, H. Huang, R. Li, X. Sun, Water-Mediated Synthesis of a Superionic Halide Solid Electrolyte, Angew. Chem., Int. Ed. 58 (2019) 16427–16432, https://doi.org/10.1002/anie.201909805.

[41] S. Yu, J. Noh, B. Kim, J.-H. Song, K. Oh, J. Yoo, S. Lee, S.-O. Park, W. Kim, B. Kang, D. Kil, K. Kang, Design of A Trigonal Halide Superionic Conductor by Regulating Cation Order-Disorder, Science 382 (2023) 573–579, https://doi.org/10.1126/science.adg6591.

[42] A. Sakuda, A. Hayashi, M. Tatsumisago, Sulfide Solid Electrolyte with Favorable Mechanical Property for All-Solid-State Lithium Battery, Sci. Rep. 3 (2013) 2261, https://doi.org/10.1038/srep02261.

[43] K.H. Park, Q. Bai, D.H. Kim, D.Y. Oh, Y. Zhu, Y. Mo, Y.S. Jung, Design Strategies, Practical Considerations, and New Solution Processes of Sulfide Solid Electrolytes for All-Solid-State Batteries, Adv. Energy Mater. 8 (2018) 1800035, https://doi.org/10.1002/aenm.201800035.

[44] J.G. Smith, D.J. Siegel, Low-Temperature Paddlewheel Effect in Glassy Solid Slectrolytes, Nat. Commun. 11 (2020) 1483, https://doi.org/10.1038/s41467-020-15245-5.

[45] Z. Zhang, L.F. Nazar, Exploiting The Paddle-Wheel Mechanism for The Design of Fast Ion Conductors, Nat. Rev. Mater. 7 (2022) 389–405, https://doi.org/10.1038/s41578-021-00401-0.

[46] I. Hanghofer, M. Brinek, S.L. Eisbacher, B. Bitschnau, M. Volck, V. Hennige, I. Hanzu, D. Rettenwander, H.M.R. Wilkening, Substitutional Disorder: Structure and Ion Dynamics of The Argyrodites Li_6PS_5Cl, Li_6PS_5Br and Li_6PS_5I, Phys. Chem. Chem. Phys. 21 (2019) 8489–8507, https://doi.org/10.1039/C9CP00664H.

[47] H. Huo, Y. Chen, J. Luo, X. Yang, X. Guo, X. Sun, Rational Design of Hierarchical "Ceramic-in-Polymer" and "Polymer-in-Ceramic" Electrolytes for Dendrite-Free Solid-State Batteries, Adv. Energy Mater. 9 (2019) 1804004, https://doi.org/10.1002/aenm.201804004.

[48] J. Haruyama, K. Sodeyama, L. Han, K. Takada, Y. Tateyama, Space–Charge Layer Effect at Interface between Oxide Cathode and Sulfide Electrolyte in All-Solid-State Lithium-Ion Battery, Chem. Mater. 26 (2014) 4248–4255, https://doi.org/10.1021/cm5016959.

[49] X. Lu, Y. Wang, X. Xu, B. Yan, T. Wu, L. Lu, Polymer-Based Solid-State Electrolytes for High-Energy-Density Lithium-Ion Batteries – Review, Adv. Energy Mater. 13 (2023) 2301746, https://doi.org/10.1002/aenm.202301746.

[50] Y.-F. Huang, J.-P. Zeng, S.-F. Li, C. Dai, J.-F. Liu, C. Liu, Y.-B. He, Conformational Regulation of Dielectric Poly(Vinylidene Fluoride)-Based Solid-State Electrolytes for Efficient Lithium Salt Dissociation and Lithium-Ion Transportation, Adv. Energy Mater. 13 (2023) 2203888, https://doi.org/10.1002/aenm.202203888.

[51] S. Xue, S. Chen, Y. Fu, H. Zhu, Y. Ji, Y. Song, F. Pan, L. Yang, Revealing the Role of Active Fillers in Li-ion Conduction of Composite Solid Electrolytes, Small 19 (2023) 2305326, https://doi.org/10.1002/smll.202305326.

[52] C. Shi, J. Song, Y. Zhang, X. Wang, Z. Jiang, T. Sun, J. Zhao, Revealing the Mechanisms of Lithium-Ion Transport and Conduction in Composite Solid Polymer Electrolytes, Cell. Rep. Phys. Sci. 4 (2023) 101321, https://doi.org/10.1016/j.xcrp.2023.101321.

[53] D. Lin, Y. Liu, Y. Cui, Reviving the Lithium Metal Anode For High-Energy Batteries, Nat. Nanotechnol. 12 (2017) 194–206, https://doi.org/10.1038/nnano.2017.16.

[54] Z. Ma, A. Song, Z. Liu, Y. Guo, X. Yang, Q. Li, Y. Fan, L. Dai, H. Tian, X. Qin, H. Liu, G. Shao, G. Wang, Nanoconfined Expansion Behavior of Hollow MnS@Carbon Anode with Extended Lithiation Cyclic Stability, Adv. Funct. Mater. 33 (2023) 2301112, https://doi.org/10.1002/adfm.202301112.

[55] D.K. Singh, A. Henss, B. Mogwitz, A. Gautam, J. Horn, T. Krauskopf, S. Burkhardt, J. Sann, F.H. Richter, J. Janek, Li_6PS_5Cl Microstructure and Influence on Dendrite Growth in Solid-State Batteries with Lithium Metal Anode, Cell. Rep. Phys. Sci. 3 (2022) 101043, https://doi.org/10.1016/j.xcrp.2022.101043.

[56] X. Fan, X. Ou, W. Zhao, Y. Liu, B. Zhang, J. Zhang, L. Zou, L. Seidl, Y. Li, G. Hu, C. Battaglia, Y. Yang, In Situ Inorganic Conductive Network Formation in High-Voltage Single-Crystal Ni-Rich Cathodes, Nat. Commun. 12 (2021) 5320, https://doi.org/10.1038/s41467-021-25611-6.

[57] H.B. Lee, T. Dinh Hoang, Y.S. Byeon, H. Jung, J. Moon, M.-S. Park, Surface Stabilization of Ni-Rich Layered Cathode Materials via Surface Engineering with $LiTaO_3$ for Lithium-Ion Batteries, ACS Appl. Mater. Interfaces 14 (2022) 2731–2741, https://doi.org/10.1021/acsami.1c19443.

[58] L. Wang, T. Liu, T. Wu, J. Lu, Strain-Retardant Coherent Perovskite Phase Stabilized Ni-rich Cathode, Nature 611 (2022) 61–67, https://doi.org/10.1038/s41586-022-05238-3.

[59] Y. Lu, C.-Z. Zhao, J.-K. Hu, S. Sun, H. Yuan, Z.-H. Fu, X. Chen, J.-Q. Huang, M. Ouyang, Q. Zhang, The Void Formation Behaviors in Working Solid-State Li Metal Batteries, Sci. Adv. 8 (2022) eadd0510, https://doi.org/10.1126/sciadv.add0510.

[60] H. Yan, K. Tantratian, K. Ellwood, E.T. Harrison, M. Nichols, X. Cui, L. Chen, How Does the Creep Stress Regulate Void Formation at the Lithium-Solid Electrolyte Interface during Stripping? Adv. Energy Mater. 12 (2022) 2102283 https://doi.org/10.1002/aenm.202102283.

[61] H.-H. Ryu, K.-J. Park, C.S. Yoon, Y.-K. Sun, Capacity Fading of Ni-Rich Li $[Ni_xCo_yMn_{1-x-y}]O_2$ ($0.6 \leq x \leq 0.95$) Cathodes for High-Energy-Density Lithium-Ion Batteries: Bulk or Surface Degradation? Chem. Mater. 30 (2018) 1155–1163, https://doi.org/10.1021/acs.chemmater.7b05269.

[62] Y. He, C. Lu, S. Liu, W. Zheng, J. Luo, Interfacial Incompatibility and Internal Stresses in All-Solid-State Lithium Ion Batteries, Adv. Energy Mater. 9 (2019) 1901810, https://doi.org/10.1002/aenm.201901810.

[63] Z. Ning, G. Li, D.L.R. Melvin, Y. Chen, J. Bu, D. Spencer-Jolly, J. Liu, B. Hu, X. Gao, J. Perera, C. Gong, S.D. Pu, S. Zhang, B. Liu, G.O. Hartley, A.J. Bodey, R. I. Todd, P.S. Grant, D.E.J. Armstrong, T.J. Marrow, C.W. Monroe, P.G. Bruce, Dendrite Initiation and Propagation in Lithium Metal Solid-State Batteries, Nature 618 (2023) 287–293, https://doi.org/10.1038/s41586-023-05970-4.

[64] W. Wang, J. Wang, C. Lin, H. Ruan, Modeling of Void-Mediated Cracking and Lithium Penetration in All-Solid-State Batteries, Adv. Funct. Mater. 33 (2023) 2303484, https://doi.org/10.1002/adfm.202303484.

[65] Y. Bi, J. Tao, Y. Wu, L. Li, Y. Xu, E. Hu, B. Wu, J. Hu, C. Wang, J.-G. Zhang, Y. Qi, J. Xiao, Reversible Planar Gliding and Microcracking in a Single-Crystalline Ni-Rich Cathode, Science 370 (2020) 1313–1317, https://doi.org/10.1126/science.abc3167.

[66] A. Banerjee, X. Wang, C. Fang, E.A. Wu, Y.S. Meng, Interfaces and Interphases in All-Solid-State Batteries with Inorganic Solid Electrolytes, Chem. Rev. 120 (2020) 6878–6933, https://doi.org/10.1021/acs.chemrev.0c00101.

[67] D. Cao, T. Ji, A. Singh, S. Bak, Y. Du, X. Xiao, H. Xu, J. Zhu, H. Zhu, Unveiling the Mechanical and Electrochemical Evolution of Nanosilicon Composite Anodes in Sulfide-Based All-Solid-State Batteries, Adv. Energy Mater. 13 (2023) 2203969, https://doi.org/10.1002/aenm.202203969.

[68] C. Zheng, J. Zhang, Y. Xia, H. Huang, Y. Gan, C. Liang, X. He, X. Tao, W. Zhang, Unprecedented Self-Healing Effect of Li_6PS_5Cl-Based All-Solid-State Lithium Battery, Small 17 (2021) 2101326, https://doi.org/10.1002/smll.202101326.

[69] D. Zeng, J. Yao, L. Zhang, R. Xu, S. Wang, X. Yan, C. Yu, L. Wang, Promoting Favorable Interfacial Properties in Lithium-Based Batteries using Chlorine-Rich Sulfide Inorganic Solid-State Electrolytes, Nat. Commun. 13 (2022) 1909, https://doi.org/10.1038/s41467-022-29596-8.

[70] G.F. Dewald, S. Ohno, M.A. Kraft, R. Koerver, P. Till, N.M. Vargas-Barbosa, J. Janek, W.G. Zeier, Experimental Assessment of the Practical Oxidative Stability of Lithium Thiophosphate Solid Electrolytes, Chem. Mater. 31 (2019) 8328–8337, https://doi.org/10.1021/acs.chemmater.9b01550.

[71] F. Han, T. Gao, Y. Zhu, K.J. Gaskell, C. Wang, A Battery Made from a Single Material, Adv. Mater. 27 (2015) 3473–3483, https://doi.org/10.1002/adma.201500180.

[72] T. Swamy, X. Chen, Y.-M. Chiang, Electrochemical Redox Behavior of Li Ion Conducting Sulfide Solid Electrolytes, Chem. Mater. 31 (2019) 707–713, https://doi.org/10.1021/acs.chemmater.8b03420.

[73] Y. Aizawa, K. Yamamoto, T. Sato, H. Murata, R. Yoshida, C.A.J. Fisher, T. Kato, Y. Iriyama, T. Hirayama, In Situ Electron Holography of Electric Potentials Inside a Solid-State Electrolyte: Effect of Electric-Field Leakage, Ultramicroscopy 178 (2017) 20–26, https://doi.org/10.1016/j.ultramic.2016.07.015.

[74] H. Masuda, N. Ishida, Y. Ogata, D. Ito, D. Fujita, Internal Potential Mapping of Charged Solid-State-Lithium Ion Batteries using In Situ Kelvin Probe Force Microscopy, Nanoscale 9 (2017) 893–898, https://doi.org/10.1039/C6NR07971G.

[75] K. Takada, N. Ohta, L. Zhang, X. Xu, B.T. Hang, T. Ohnishi, M. Osada, T. Sasaki, Interfacial Phenomena in Solid-State Lithium Battery with Sulfide Solid Electrolyte, Solid State Ion.-. 225 (2012) 594–597, https://doi.org/10.1016/j.ssi.2012.01.009.

[76] K. Yamamoto, Y. Iriyama, T. Asaka, T. Hirayama, H. Fujita, C.A.J. Fisher, K. Nonaka, Y. Sugita, Z. Ogumi, Dynamic Visualization of the Electric Potential in an All-Solid-State Rechargeable Lithium Battery, Angew. Chem., Int. Ed. 49 (2010) 4414–4417, https://doi.org/10.1002/anie.200907319.

[77] Z. Cheng, M. Liu, S. Ganapathy, C. Li, Z. Li, X. Zhang, P. He, H. Zhou, M. Wagemaker, Revealing the Impact of Space-Charge Layers on the Li-Ion Transport in All-Solid-State Batteries, Joule 4 (2020) 1311–1323, https://doi.org/10.1016/j.joule.2020.04.002.

[78] M. Fingerle, R. Buchheit, S. Sicolo, K. Albe, R. Hausbrand, Reaction and Space Charge Layer Formation at the LiCoO2–LiPON Interface: Insights on Defect Formation and Ion Energy Level Alignment by a Combined Surface Science–Simulation Approach, Chem. Mater. 29 (2017) 7675–7685, https://doi.org/10.1021/acs.chemmater.7b00890.

[79] K. Leung, A.J. Pearse, A.A. Talin, E.J. Fuller, G.W. Rubloff, N.A. Modine, Kinetics-Controlled Degradation Reactions at Crystalline LiPON/$LixCoO_2$ and Crystalline LiPON/Li-Metal Interfaces, ChemSusChem 11 (2018) 1956–1969, https://doi.org/10.1002/cssc.201800027.

[80] N. Sata, K. Eberman, K. Eberl, J. Maier, Mesoscopic Fast Ion Conduction in Nanometre-Scale Planar Heterostructures, Nature 408 (2000) 946–949, https://doi.org/10.1038/35050047.

[81] J. Maier, Nanoionics: Ionic Charge Carriers in Small Systems, Phys. Chem. Chem. Phys. 11 (2009) 3011–3022, https://doi.org/10.1039/B902586N.

[82] L. Wang, R. Xie, B. Chen, X. Yu, J. Ma, C. Li, Z. Hu, X. Sun, C. Xu, S. Dong, T.-S. Chan, J. Luo, G. Cui, L. Chen, In-Situ Visualization of the Space-Charge-Layer Effect on Interfacial Lithium-Ion Transport in All-Solid-State Batteries, Nat. Commun. 11 (2020) 5889, https://doi.org/10.1038/s41467-020-19726-5.

[83] N.J.J. de Klerk, M. Wagemaker, Space-Charge Layers in All-Solid-State Batteries; Important or Negligible? ACS Appl. Energy Mater. 1 (2018) 5609–5618, https://doi.org/10.1021/acsaem.8b01141.

[84] L. Fu, C.-C. Chen, D. Samuelis, J. Maier, Thermodynamics of Lithium Storage at Abrupt Junctions: Modeling and Experimental Evidence, Phys. Rev. Lett. 112 (2014) 208301, https://doi.org/10.1103/PhysRevLett.112.208301.

[85] S. Stegmaier, J. Voss, K. Reuter, A.C. Luntz, Li^+ Defects in a Solid-State Li Ion Battery: Theoretical Insights with a Li_3OCl Electrolyte, Chem. Mater. 29 (2017) 4330–4340, https://doi.org/10.1021/acs.chemmater.7b00659.

[86] M.W. Swift, Y. Qi, First-Principles Prediction of Potentials and Space-Charge Layers in All-Solid-State Batteries, Phys. Rev. Lett. 122 (2019) 167701, https://doi.org/10.1103/PhysRevLett.122.167701.

[87] Y. Nomura, K. Yamamoto, T. Hirayama, S. Ouchi, E. Igaki, K. Saitoh, Direct Observation of a Li-Ionic Space-Charge Layer Formed at an Electrode/Solid-Electrolyte Interface, Angew. Chem., Int. Ed. 58 (2019) 5292–5296, https://doi.org/10.1002/anie.201814669.

[88] Z. Gu, J. Ma, F. Zhu, T. Liu, K. Wang, C.-W. Nan, Z. Li, C. Ma, Atomic-Scale Study Clarifying the Role of Space-Charge Layers in a Li-Ion-Conducting Solid Electrolyte, Nat. Commun. 14 (2023) 1632, https://doi.org/10.1038/s41467-023-37313-2.

[89] S. Anada, K. Yamamoto, H. Sasaki, N. Shibata, M. Matsumoto, Y. Hori, K. Kinugawa, A. Imamura, T. Hirayama, Accurate Measurement of Electric Potentials in Biased GaAs Compound Semiconductors by Phase-Shifting Electron Holography, Microscopy 68 (2019) 159–166, https://doi.org/10.1093/jmicro/dfy131.

[90] Z. Yang, M. Li, G. Lu, Y. Wang, J. Wei, X. Hu, Z. Li, P. Li, C. Xu, High-Performance Composite Lithium Anodes Enabled by Electronic/Ionic Dual-Conductive Paths for Solid-State Li Metal Batteries, Small 18 (2022) 2202911, https://doi.org/10.1002/smll.202202911.

[91] D. Guo, D.B. Shinde, W. Shin, E. Abou-Hamad, A.-H. Emwas, Z. Lai, A. Manthiram, Foldable Solid-State Batteries Enabled by Electrolyte Mediation in Covalent Organic Frameworks, Adv. Mater. 34 (2022) 2201410, https://doi.org/10.1002/adma.202201410.

[92] J. Zheng, C. Sun, Z. Wang, S. Liu, B. An, Z. Sun, F. Li, Double Ionic–Electronic Transfer Interface Layers for All-Solid-State Lithium Batteries, Angew. Chem., Int. Ed. 60 (2021) 18448–18453, https://doi.org/10.1002/anie.202104183.

[93] M. Du, Y. Sun, B. Liu, B. Chen, K. Liao, R. Ran, R. Cai, W. Zhou, Z. Shao, Smart Construction of an Intimate Lithium | Garnet Interface for All-Solid-State Batteries by Tuning the Tension of Molten Lithium, Adv. Funct. Mater. 31 (2021) 2101556, https://doi.org/10.1002/adfm.202101556.

[94] L. Nie, S. Chen, C. Zhang, L. Dong, Y. He, T. Gao, J. Yu, W. Liu, Integration of a Low-Tortuous Electrode and an In-Situ-Polymerized Electrolyte for All-Solid-State Lithium-Metal Batteries, Cell. Rep. Phys. Sci. 3 (2022) 100851, https://doi.org/10.1016/j.xcrp.2022.100851.

[95] G.V. Alexander, O.V. Sreejith, M.S. Indu, R. Murugan, Interface-Compatible and High-Cyclability Lithiophilic Lithium–Zinc Alloy Anodes for Garnet-Structured Solid Electrolytes, ACS Appl. Energy Mater. 3 (2020) 9010–9017, https://doi.org/10.1021/acsaem.0c01430.

[96] T. Famprikis, P. Canepa, J.A. Dawson, M.S. Islam, C. Masquelier, Fundamentals of Inorganic Solid-State Electrolytes for Batteries, Nat. Mater. 18 (2019) 1278–1291, https://doi.org/10.1038/s41563-019-0431-3.
[97] C. Wang, T. Deng, X. Fan, M. Zheng, R. Yu, Q. Lu, H. Duan, H. Huang, C. Wang, X. Sun, Identifying Soft Breakdown in All-Solid-State Lithium Battery, Joule 6 (2022) 1770–1781, https://doi.org/10.1016/j.joule.2022.05.020.
[98] F.M. Pesci, A. Bertei, R.H. Brugge, S.P. Emge, A.K.O. Hekselman, L.E. Marbella, C. P. Grey, A. Aguadero, Establishing Ultralow Activation Energies for Lithium Transport in Garnet Electrolytes, ACS Appl. Mater. Interfaces 12 (2020) 32806–32816, https://doi.org/10.1021/acsami.0c08605.
[99] N.C. Rosero-Navarro, R. Kajiura, R. Jalem, Y. Tateyama, A. Miura, K. Tadanaga, Significant Reduction in the Interfacial Resistance of Garnet-Type Solid Electrolyte and Lithium Metal by a Thick Amorphous Lithium Silicate Layer, ACS Appl. Energy Mater. 3 (2020) 5533–5541, https://doi.org/10.1021/acsaem.0c00511.
[100] C. Cao, Y. Zhong, K. Chandula Wasalathilake, M.O. Tadé, X. Xu, H. Rabiee, M. Roknuzzaman, R. Rahman, Z. Shao, A Low Resistance and Stable Lithium-Garnet Electrolyte Interface Enabled by a Multifunctional Anode Additive for Solid-State Lithium Batteries, J. Mater. Chem. A 10 (2022) 2519–2527, https://doi.org/10.1039/D1TA07804F.
[101] G. Lu, M. Li, P. Chen, W. Zheng, Z. Yang, R. Wang, C. Xu, Built-in Superionic Conductive Phases Enabling Dendrite-free, Long Lifespan and High Specific Capacity Composite Lithium for Stable Solid-State Lithium Batteries, Energy Environ. Sci. 16 (2023) 1049–1061, https://doi.org/10.1039/D2EE03709B.
[102] Y. Zhong, C. Cao, M.O. Tadé, Z. Shao, Ionically and Electronically Conductive Phases in a Composite Anode for High-Rate and Stable Lithium Stripping and Plating for Solid-State Lithium Batteries, ACS Appl. Mater. Interfaces 14 (2022) 38786–38794, https://doi.org/10.1021/acsami.2c09801.
[103] Y.L. Yap, A.H. You, L.L. Teo, Preparation and Characterization Studies of PMMA–PEO-blend Solid Polymer Electrolytes with SiO_2 Filler and Plasticizer for Lithium Ion Battery, Ionics 25 (2019) 3087–3098, https://doi.org/10.1007/s11581-019-02842-8.
[104] J.-C. Guo, S.-J. Tan, C.-H. Zhang, W.-P. Wang, Y. Zhao, F. Wang, X.-S. Zhang, R. Wen, Y. Zhang, M. Fan, S. Xin, J. Zhang, Y.-G. Guo, A Self-Reconfigured, Dual-Layered Artificial Interphase Toward High-Current-Density Quasi-Solid-State Lithium Metal Batteries, e2300350-e2300350, Adv. Mater. 35 (2023), https://doi.org/10.1002/adma.202300350.
[105] T. Luo, L. Wang, L. Dai, J. Luo, S. Liu, A Solid-State Lithium Metal Battery with Extended Cycling and Rate Performance using a Low-Melting Alloy Interface, Inorg. Chem. Front. 10 (2023) 1011–1017, https://doi.org/10.1039/D2QI02127G.
[106] T. Deng, X. Ji, Y. Zhao, L.S. Cao, S. Li, S. Hwang, C. Luo, P.F. Wang, H.P. Jia, X. L. Fan, X.C. Lu, D. Su, X.L. Sun, C.S. Wang, J.G. Zhang, Tuning the Anode-Electrolyte Interface Chemistry for Garnet-Based Solid-State Li Metal Batteries, Adv. Mater. 32 (2020) 2000030, https://doi.org/10.1002/adma.202000030.
[107] T. Luo, B. Liu, W. Han, G. Zhu, J. Liang, L. Wang, J. Yang, L. Wang, S. Liu, Enhanced Ion-Electron Mixing Interface for High Energy Solid-State Lithium Metal Batteries, J. Colloid Interface Sci. 652 (2023) 1085–1091, https://doi.org/10.1016/j.jcis.2023.08.119.
[108] F. Chen, J. Luo, M.-x Jing, J. Li, Z.-h Huang, H. Yang, X.-q Shen, A Sandwich Structure Composite Solid Electrolyte with Enhanced Interface Stability and Electrochemical Properties For Solid-state Lithium Batteries, J. Electrochem. Soc. 168 (2021) 070513, https://doi.org/10.1149/1945-7111/ac0f89.
[109] H. Wang, C. Wang, M. Zheng, J. Liang, M. Yang, X. Feng, X. Ren, D.Y.W. Yu, Y. Li, X. Sun, A Shuttle-Free Solid-State Cu−Li Battery Based on a Sandwich-Structured Electrolyte, Angew. Chem., Int. Ed. 62 (2023) e202214117, https://doi.org/10.1002/anie.202214117.
[110] M. Lei, S. Fan, Y. Yu, J. Hu, K. Chen, Y. Gu, C. Wu, Y. Zhang, C. Li, NASICON-based Solid State Li-Fe-F Conversion Batteries Enabled by Multi-Interface-Compatible Sericin Protein Buffer Layer, Energy Storage Mater. 47 (2022) 551–560, https://doi.org/10.1016/j.ensm.2022.02.031.
[111] S. Zhang, Q. Sun, G. Hou, J. Cheng, L. Dai, J. Li, L. Ci, Boosting fast interfacial Li^+ transport in solid-state Li metal batteries via ultrathin Al buffer layer, Nano Res 16 (2022) 6825–6832, https://doi.org/10.1007/s12274-022-5345-8.
[112] C. Li, Y. Chen, Z. Li, Y. Zhang, Z. Fang, J. Xu, Y. Sun, H. Bao, H. Cheng, Construction of Sticky Ionic Conductive Buffer Layer for Inorganic Electrolyte Toward Stable All-Solid-State Lithium Metal Batteries, J. Power Sources 495 (2021) 229765, https://doi.org/10.1016/j.jpowsour.2021.229765.
[113] C. Duan, Z. Cheng, W. Li, F. Li, H. Liu, J. Yang, G. Hou, P. He, H. Zhou, Realizing the Compatibility of a Li Metal Anode in An All-Solid-State Li−S Battery by Chemical Iodine–Capor Deposition, Energy Environ. Sci. 15 (2022) 3236–3245, https://doi.org/10.1039/D2EE01358D.
[114] W. Zhou, S. Wang, Y. Li, S. Xin, A. Manthiram, J.B. Goodenough, Plating a Dendrite-Free Lithium Anode with a Polymer/Ceramic/Polymer Sandwich Electrolyte, J. Am. Chem. Soc. 138 (2016) 9385–9388, https://doi.org/10.1021/jacs.6b05341.
[115] M. Chen, X. Fu, Z. Chen, J. Liu, W.-H. Zhong, Protein-Engineered Functional Materials for Bioelectronics, Adv. Funct. Mater. 31 (2021) 2006744, https://doi.org/10.1002/adfm.202006744.
[116] L. Cheng, Z. Cai, T. Ye, X. Yu, Z. Chen, Y. Yan, J. Qi, L. Wang, Z. Liu, W. Cui, L. Deng, Injectable Polypeptide-Protein Hydrogels for Promoting Infected Wound Healing, Adv. Funct. Mater. 30 (2020) 2001196, https://doi.org/10.1002/adfm.202001196.
[117] D. Wang, H. Xiea, Q. Liu, K. Mu, Z. Song, W. Xu, L. Tian, C. Zhu, J. Xu, Low-Cost, High-Strength Cellulose-based Quasi-Solid Polymer Electrolyte for Solid-State Lithium-Metal Batteries, Angew. Chem., Int. Ed. 62 (2023) e202302767, https://doi.org/10.1002/anie.202302767.
[118] W. Zhang, H.L. Zhuang, L. Fan, L. Gao, Y. Lu, A "Cation-Anion Regulation" Synergistic Anode Host for Dendrite-Free Lithium Metal Batteries, Sci. Adv. 4 (2018) eaar4410, https://doi.org/10.1126/sciadv.aar4410.
[119] Y.-K. Liao, Z. Tong, C.-C. Fang, S.-C. Liao, J.-M. Chen, R.-S. Liu, S.-F. Hu, Extensively Reducing Interfacial Resistance by the Ultrathin Pt Layer between the Garnet-Type Solid-State Electrolyte and Li–Metal Anode, ACS Appl. Mater. Interfaces 13 (2021) 56181–56190, https://doi.org/10.1021/acsami.1c16922.
[120] H.-K. Tian, R. Jalem, B. Gao, Y. Yamamoto, S. Muto, M. Sakakura, Y. Iriyama, Y. Tateyama, Electron and Ion Transfer across Interfaces of the NASICON-Type LATP Solid Electrolyte with Electrodes in All-Solid-State Batteries: A Density Functional Theory Study via an Explicit Interface Model, ACS Appl. Mater. Interfaces 12 (2020) 54752–54762, https://doi.org/10.1021/acsami.0c16463.
[121] Q. Cheng, A. Li, N. Li, S. Li, A. Zangiabadi, T.-D. Li, W. Huang, A.C. Li, T. Jin, Q. Song, W. Xu, N. Ni, H. Zhai, M. Dontigny, K. Zaghib, X. Chuan, D. Su, K. Yan, Y. Yang, Stabilizing Solid Electrolyte-Anode Interface in Li-Metal Batteries by Boron Nitride-Based Nanocomposite Coating, Joule 3 (2019) 1510–1522, https://doi.org/10.1016/j.joule.2019.03.022.
[122] K. Shi, Z. Wan, L. Yang, Y. Zhang, Y. Huang, S. Su, H. Xia, K. Jiang, L. Shen, Y. Hu, S. Zhang, J. Yu, F. Ren, Y.-B. He, F. Kang, InSitu Construction of an Ultra-Stable Conductive Composite Interface for High-Voltage All-Solid-State Lithium Metal Batteries, Angew. Chem., Int. Ed. 59 (2020) 11784–11788, https://doi.org/10.1002/anie.202000547.
[123] N. Ci, L. Zhang, J. Li, D. Li, J. Cheng, Q. Sun, Z. Xi, Z. Xu, G. Zhao, L. Ci, In Situ Construction of a Flexible Interlayer for Durable Solid-State Lithium Metal Batteries, Carbon 187 (2022) 13–21, https://doi.org/10.1016/j.carbon.2021.10.070.
[124] S. Guo, T.-T. Wu, Y.-G. Sun, S.-D. Zhang, B. Li, H.-S. Zhang, M.-Y. Qi, X.-H. Liu, A.-M. Cao, L.-J. Wan, Interface Engineering of a Ceramic Electrolyte by Ta_2O_5 Nanofilms for Ultrastable Lithium Metal Batteries, Adv. Funct. Mater. 32 (2022) 2201498, https://doi.org/10.1002/adfm.202201498.
[125] X. Gao, W. Yuan, Y. Yang, Y. Wu, C. Wang, X. Wu, X. Zhang, Y. Yuan, Y. Tang, Y. Chen, C. Yang, B. Zhao, High-Performance and Highly Safe Solvate Ionic Liquid-Based Gel Polymer Electrolyte by Rapid UV-Curing for Lithium-Ion Batteries, ACS Appl. Mater. Interfaces 14 (2022) 43397–43406, https://doi.org/10.1021/acsami.2c13325.
[126] H. Hu, W. Yuan, H. Zhao, G.L. Baker, A novel polymer gel electrolyte: Direct Polymerization of Ionic Liquid from Surface of Silica Nanoparticles, J. Polym. Sci. Part A: Polym. Chem. 52 (2014) 121–127, https://doi.org/10.1002/pola.26980.
[127] A.S. Shaplov, E.I. Lozinskaya, I.L. Odinets, K.A. Lyssenko, S.A. Kurtova, G. I. Timofeeva, C. Iojoiu, J.-Y. Sanchez, M.J.M. Abadie, V.Y. Voytekunas, Y. S. Vygodskii, Novel Phosphonated Poly(1,3,4-oxadiazole)s: Synthesis in Ionic Liquid and Characterization, React. Funct. Polym. 68 (2008) 208–224, https://doi.org/10.1016/j.reactfunctpolym.2007.09.001.
[128] J. Yi, C. Yan, D. Zhou, L.-Z. Fan, A robust solid electrolyte interphase enabled by solvate ionic liquid for high-performance sulfide-based all-solid-state lithium metal batteries, Nano Res 16 (2022) 8411–8416, https://doi.org/10.1007/s12274-022-5304-4.
[129] M. Liu, S. Zhang, E.R.H. van Eck, C. Wang, S. Ganapathy, M. Wagemaker, Improving Li-ion Interfacial Transport in Hybrid Solid Electrolytes, Nat. Nanotechnol. 17 (2022) 959–967, https://doi.org/10.1038/s41565-022-01162-9.
[130] D. Yu, Z. Ma, Z. Liu, X. Jiang, H.A. Younus, X. Wang, S. Zhang, Optimizing Interfacial Wetting by Ionic Liquid for High Performance Solid-State Lithium Metal Batteries Operated at Ambient Temperature, Chem. Eng. J. 457 (2023) 141043, https://doi.org/10.1016/j.cej.2022.141043.
[131] C. Fu, G. Homann, R. Grissa, D. Rentsch, W. Zhao, T. Gouveia, A. Falgayrat, R. Lin, S. Fantini, C. Battaglia, A Polymerized-Ionic-Liquid-Based Polymer Electrolyte with High Oxidative Stability for 4 and 5 V Class Solid-State Lithium Metal Batteries, Adv. Energy Mater. 12 (2022) 2200412, https://doi.org/10.1002/aenm.202200412.
[132] Y. Yuan, X. Peng, B. Wang, K. Xue, Z. Li, Y. Ma, B. Zheng, Y. Song, H. Lu, Solvate Ionic Liquid-Derived Solid Polymer Electrolyte with Lithium Bis(oxalato) borate as a Functional Additive for Solid-State Lithium Metal Batteries, J. Mater. Chem. A 11 (2023) 1301–1311, https://doi.org/10.1039/D2TA07393E.
[133] Y. Lu, Z. Tu, L.A. Archer, Stable Lithium Electrodeposition in Liquid and Nanoporous Solid Electrolytes, Nat. Mater. 13 (2014) 961–969, https://doi.org/10.1038/nmat4041.
[134] J. Tan, J. Matz, P. Dong, J. Shen, M. Ye, A Growing Appreciation for the Role of LiF in the Solid Electrolyte Interphase, Adv. Energy Mater. 11 (2021) 2100046, https://doi.org/10.1002/aenm.202100046.
[135] K. Liu, Z. Wang, L. Shi, S. Jungsuttiwong, S. Yuan, Ionic Liquids for High Performance Lithium Metal Batteries, J. Energy Chem. 59 (2021) 320–333, https://doi.org/10.1016/j.jechem.2020.11.017.
[136] Z. Wang, F. Zhang, Y. Sun, L. Zheng, Y. Shen, D. Fu, W. Li, A. Pan, L. Wang, J. Xu, J. Hu, X. Wu, Intrinsically Nonflammable Ionic Liquid-Based Localized Highly Concentrated Electrolytes Enable High-Performance Li-Metal Batteries, Adv. Energy Mater. 11 (2021) 2003752, https://doi.org/10.1002/aenm.202003752.
[137] L. Zhu, Y. Wang, Y. Wu, W. Feng, Z. Liu, W. Tang, X. Wang, Y. Xia, Boron Nitride-Based Release Agent Coating Stabilizes $Li_{1.3}Al_{0.3}Ti_{1.7}(PO_4)_3$/Li Interface with Superior Lean-Lithium Electrochemical Performance and Thermal Stability, Adv. Funct. Mater. 32 (2022) 2201136, https://doi.org/10.1002/adfm.202201136.
[138] P. Zhai, Z. Yang, Y. Wei, X. Guo, Y. Gong, Two-Dimensional Fluorinated Graphene Reinforced Solid Polymer Electrolytes for High-Performance Solid-State Lithium Batteries, Adv. Energy Mater. 12 (2022) 2200967, https://doi.org/10.1002/aenm.202200967.

[139] Y. Gao, D. Wang, Y.C. Li, Z. Yu, T.E. Mallouk, D. Wang, Salt-Based Organic–Inorganic Nanocomposites: Towards A Stable Lithium Metal/$Li_{10}GeP_2S_{12}$ Solid Electrolyte Interface, Angew. Chem., Int. Ed. 57 (2018) 13608–13612, https://doi.org/10.1002/anie.201807304.

[140] J. Leng, H. Liang, H. Wang, Z. Xiao, S. Wang, Z. Zhang, Z. Tang, A Facile and Low-cost Wet-chemistry Artificial Interface Engineering for Garnet-based Solid-State Li Metal Batteries, Nano Energy 101 (2022) 107603, https://doi.org/10.1016/j.nanoen.2022.107603.

[141] J. Lee, S.H. Choi, G. Im, K.-J. Lee, T. Lee, J. Oh, N. Lee, H. Kim, Y. Kim, S. Lee, J. W. Choi, Room-Temperature Anode-Less All-Solid-State Batteries via the Conversion Reaction of Metal Fluorides, Adv. Mater. 34 (2022) 2203580, https://doi.org/10.1002/adma.202203580.

[142] D. Wang, T. Xie, C. Qin, X. Wang, G. Li, Y. Liu, H. Zou, L. Huang, Y. Wu, Artificial SEI Film via Synchronous Reaction-Diffusion-Assembly on Li Liquid Metal, Adv. Funct. Mater. 32 (2022) 2206405, https://doi.org/10.1002/adfm.202206405.

[143] C. Heubner, S. Maletti, H. Auer, J. Hüttl, K. Voigt, O. Lohrberg, K. Nikolowski, M. Partsch, A. Michaelis, From Lithium-Metal toward Anode-Free Solid-State Batteries: Current Developments, Issues, and Challenges, Adv. Funct. Mater. 31 (2021) 2106608, https://doi.org/10.1002/adfm.202106608.

[144] O. Sheng, J. Zheng, Z. Ju, C. Jin, Y. Wang, M. Chen, J. Nai, T. Liu, W. Zhang, Y. Liu, X. Tao, In Situ Construction of a LiF-Enriched Interface for Stable All-Solid-State Batteries and its Origin Revealed by Cryo-TEM, Adv. Mater. 32 (2020) 2000223, https://doi.org/10.1002/adma.202000223.

[145] A. Hu, W. Chen, X. Du, Y. Hu, T. Lei, H. Wang, L. Xue, Y. Li, H. Sun, Y. Yan, J. Long, C. Shu, J. Zhu, B. Li, X. Wang, J. Xiong, An Artificial Hybrid Interphase for an Ultrahigh-Rate and Practical Lithium Metal Anode, Energy Environ. Sci. 14 (2021) 4115–4124, https://doi.org/10.1039/D1EE00508A.

[146] Y.-G. Lee, S. Fujiki, C. Jung, N. Suzuki, N. Yashiro, R. Omoda, D.-S. Ko, T. Shiratsuchi, T. Sugimoto, S. Ryu, J.H. Ku, T. Watanabe, Y. Park, Y. Aihara, D. Im, I.T. Han, High-Energy Long-Cycling All-Solid-State Lithium Metal Batteries Enabled by Silver–Carbon Composite Anodes, Nat. Energy 5 (2020) 299–308, https://doi.org/10.1038/s41560-020-0575-z.

[147] R. Wang, J. Yu, J. Tang, R. Meng, L.F. Nazar, L. Huang, X. Liang, Insights into Dendrite Suppression by Alloys and the Fabrication of a Flexible Alloy-Polymer Protected Lithium Metal Anode, Energy Storage Mater. 32 (2020) 178–184, https://doi.org/10.1016/j.ensm.2020.07.039.

[148] A. Wang, J. Li, M. Yi, Y. Xie, S. Chang, H. Shi, L. Zhang, M. Bai, Y. Zhou, Y. Lai, Z. Zhang, Stable All-Solid-State Lithium Metal Batteries Enabled by Ultrathin LiF/Li_3Sb Hybrid Interface Layer, Energy Storage Mater. 49 (2022) 246–254, https://doi.org/10.1016/j.ensm.2022.04.023.

[149] Y. Liu, X. Tao, Y. Wang, C. Jiang, C. Ma, O. Sheng, G. Lu, X.W. Lou, Self-assembled Monolayers Direct a LiF-rich Interphase Toward Long-life Lithium Metal Batteries, Science 375 (2022) 739–745, https://doi.org/10.1126/science.abn1818.

[150] Q. Wang, J. Wan, X. Cao, R. Wen, Y. Guo, W. Liu, H. Zhou, Organophosphorus Hybrid Solid Electrolyte Interphase Layer Based on LixPO4 Enables Uniform Lithium Deposition for High-Performance Lithium Metal Batteries, Adv. Funct. Mater. 32 (2022) 2107923, https://doi.org/10.1002/adfm.202107923.

[151] J. Yue, J. Zhang, Y. Tong, M. Chen, L. Liu, L. Jiang, T. Lv, Y.-s Hu, H. Li, X. Huang, L. Gu, G. Feng, K. Xu, L. Suo, L. Chen, Aqueous Interphase Formed by CO_2 Brings Electrolytes Back to Salt-in-water Regime, Nat. Chem. 13 (2021) 1061–1069, https://doi.org/10.1038/s41557-021-00787-y.

[152] Z. Li, Q. He, C. Zhou, Y. Li, Z. Liu, X. Hong, X. Xu, Y. Zhao, L. Mai, Rationally Design Lithiophilic Surfaces Toward High−energy Lithium Metal Battery, Energy Storage Mater. 37 (2021) 40–46, https://doi.org/10.1016/j.ensm.2021.01.012.

[153] J. Qian, S. Wang, Y. Li, M. Zhang, F. Wang, Y. Zhao, Q. Sun, L. Li, F. Wu, R. Chen, Lithium Induced Nano-Sized Copper with Exposed Lithiophilic Surfaces to Achieve Dense Lithium Deposition for Lithium Metal Anode, Adv. Funct. Mater. 31 (2021) 2006950, https://doi.org/10.1002/adfm.202006950.

[154] Y. Xiao, L.J. Miara, Y. Wang, G. Ceder, Computational Screening of Cathode Coatings for Solid-State Batteries, Joule 3 (2019) 1252–1275, https://doi.org/10.1016/j.joule.2019.02.006.

[155] W.D. Richards, L.J. Miara, Y. Wang, J.C. Kim, G. Ceder, Interface Stability in Solid-State Batteries, Chem. Mater. 28 (2016) 266–273, https://doi.org/10.1021/acs.chemmater.5b04082.

[156] H. Tang, Z. Deng, Z. Lin, Z. Wang, I.-H. Chu, C. Chen, Z. Zhu, C. Zheng, S.P. Ong, Probing Solid–Solid Interfacial Reactions in All-Solid-State Sodium-Ion Batteries with First-Principles Calculations, Chem. Mater. 30 (2018) 163–173, https://doi.org/10.1021/acs.chemmater.7b04096.

[157] J. Shi, Z. Ma, K. Han, Q. Wan, D. Wu, X. Qu, P. Li, Coupling Novel Li_7TaO_6 Surface Buffering with Bulk Ta-Doping to Achieve Long-life Sulfide-based All-Solid-State Lithium Batteries, J. Mater. Chem. A 10 (2022) 21336–21348, https://doi.org/10.1039/D2TA06703J.

[158] Y. Liang, H. Liu, G. Wang, C. Wang, D. Li, Y. Ni, L.-Z. Fan, Heuristic Design of Cathode Hybrid Coating for Power-Limited Sulfide-Based All-Solid-State Lithium Batteries, Adv. Energy Mater. 12 (2022) 2201555, https://doi.org/10.1002/aenm.202201555.

[159] J. Liang, Y. Zhu, X. Li, J. Luo, S. Deng, Y. Zhao, Y. Sun, D. Wu, Y. Hu, W. Li, T.-K. Sham, R. Li, M. Gu, X. Sun, A Gradient Oxy-thiophosphate-coated Ni-rich Layered Oxide Cathode for Stable All-Solid-State Li-ion Batteries, Nat. Commun. 14 (2023) 146, https://doi.org/10.1038/s41467-022-35667-7.

[160] J. Zhang, H. Zhong, C. Zheng, Y. Xia, C. Liang, H. Huang, Y. Gan, X. Tao, W. Zhang, All-solid-state batteries with slurry coated $LiNi_{0.8}Co_{0.1}Mn_{0.1}O_2$ composite cathode and Li6PS5Cl electrolyte: Effect of binder content, J. Power Sources 391 (2018) 73–79, https://doi.org/10.1016/j.jpowsour.2018.04.069.

[161] S. Ito, S. Fujiki, T. Yamada, Y. Aihara, Y. Park, T.Y. Kim, S.-W. Baek, J.-M. Lee, S. Doo, N. Machida, A Rocking Chair Type All-Solid-State Lithium Ion Battery Adopting Li_2O–ZrO_2 Coated $LiNi_{0.8}Co_{0.15}Al_{0.05}O_2$ and a Sulfide Based Electrolyte, J. Power Sources 248 (2014) 943–950, https://doi.org/10.1016/j.jpowsour.2013.10.005.

[162] R.S. Negi, P. Minnmann, R. Pan, S. Ahmed, M. J. Herzog, K. Volz, R. Takata, F. Schmidt, J. Janek, M.T. Elm, Stabilizing the Cathode/Electrolyte Interface Using a Dry-Processed Lithium Titanate Coating for All-Solid-State Batteries, Chem. Mater. 33 (2021) 6713–6723, https://doi.org/10.1021/acs.chemmater.1c01123.

[163] K. Okada, N. Machida, M. Naito, T. Shigematsu, S. Ito, S. Fujiki, M. Nakano, Y. Aihara, Preparation and Electrochemical Properties of $LiAlO_2$-coated $Li(Ni_{1/3}Mn_{1/3}Co_{1/3})O_2$ for All-Solid-State Batteries, Solid State Ion.-. 255 (2014) 120–127, https://doi.org/10.1016/j.ssi.2013.12.019.

[164] S.H. Jung, K. Oh, Y.J. Nam, D.Y. Oh, P. Brüner, K. Kang, Y.S. Jung, Li_3BO_3–Li_2CO_3: Rationally Designed Buffering Phase for Sulfide All-Solid-State Li-Ion Batteries, Chem. Mater. 30 (2018) 8190–8200, https://doi.org/10.1021/acs.chemmater.8b03321.

[165] J. Li, Y. Cai, Y. Cui, H. Wu, H. Da, Y. Yang, H. Zhang, S. Zhang, Fabrication of Asymmetric Bilayer Solid-State Electrolyte with Boosted Ion Transport Enabled by Charge-rich Space Charge Layer for -20–70°C Lithium Metal Battery, Nano Energy 95 (2022) 107027, https://doi.org/10.1016/j.nanoen.2022.107027.

[166] L. Wang, B. Chen, J. Ma, G. Cui, L. Chen, Reviving Lithium Cobalt Oxide-based Lithium Secondary Batteries-Toward a Higher Energy Density, Chem. Soc. Rev. 47 (2018) 6505–6602, https://doi.org/10.1039/C8CS00322J.

[167] K. Yang, L. Chen, J. Ma, C. Lai, Y. Huang, J. Mi, J. Biao, D. Zhang, P. Shi, H. Xia, G. Zhong, F. Kang, Y.-B. He, Stable Interface Chemistry and Multiple Ion Transport of Composite Electrolyte Contribute to Ultra-long Cycling Solid-State $LiNi_{0.8}Co_{0.1}Mn_{0.1}O_2$/Lithium Metal Batteries, Angew. Chem., Int. Ed. 60 (2021) 24668–24675, https://doi.org/10.1002/anie.202110917.

[168] J. Li, J. Chen, X. Xu, Z. Wang, J. Shen, J. Sun, B. Huang, T. Zhao, Enhanced Interphase Ion Transport via Charge-Rich Space Charge Layers for Ultra-Stable Solid-State Lithium Metal Batteries, Adv. Energy Mater. 15 (2025) 2402746, https://doi.org/10.1002/aenm.202402746.

[169] C. Shen, W. Feng, Y. Yu, H. Wang, Y. Cheng, C. Dong, J. Gu, A. Zheng, X. Liao, X. Xu, L. Mai, In Situ Polymerization Inhibiting Electron Localization in Hybrid Electrolyte for Room-Temperature Solid-State Lithium Metal Batteries, Adv. Energy Mater. 14 (2024) 2304511, https://doi.org/10.1002/aenm.202304511.

[170] W. Li, S. Zhang, W. Zheng, J. Ma, L. Li, Y. Zheng, D. Sun, Z. Wen, Z. Liu, Y. Wang, G. Zhang, G. Cui, Self-Polarized Organic–Inorganic Hybrid Ferroelectric Cathode Coatings Assisted High Performance All-Solid-State Lithium Battery, Adv. Funct. Mater. 33 (2023) 2300791, https://doi.org/10.1002/adfm.202300791.

[171] B.K. Park, H. Kim, K.S. Kim, H.-S. Kim, S.H. Han, J.-S. Yu, H.J. Hah, J. Moon, W. Cho, K.J. Kim, Interface Design Considering Intrinsic Properties of Dielectric Materials to Minimize Space-Charge Layer Effect between Oxide Cathode and Sulfide Solid Electrolyte in All-Solid-State Batteries, Adv. Energy Mater. 12 (2022) 2201208, https://doi.org/10.1002/aenm.202201208.

[172] Y.Q. Mi, W. Deng, C. He, O. Eksik, Y.P. Zheng, D.K. Yao, X.B. Liu, Y.H. Yin, Y.S. Li, B.Y. Xia, Z.P. Wu, In Situ Polymerized 1,3-Dioxolane Electrolyte for Integrated Solid-State Lithium Batteries, Angew. Chem., Int. Ed. 62 (2023) e202218621, https://doi.org/10.1002/anie.202218621.

[173] H. Kim, C. Im, S. Ryu, Y.J. Gong, J. Cho, S. Pyo, H. Yun, J. Lee, J. Yoo, Y.S. Kim, Interface Modeling via Tailored Energy Band Alignment: Toward Electrochemically Stabilized All-Solid-State Li-Metal Batteries, Adv. Funct. Mater. 32 (2022) 2107555, https://doi.org/10.1002/adfm.202107555.

[174] Z. Dai, J. Wang, H. Zhao, Y. Bai, Surface Coupling between Mechanical and Electric Fields Empowering Ni-Rich Cathodes with Superior Cyclabilities for Lithium-Ion Batteries, Adv. Sci. 9 (2022) 2200622, https://doi.org/10.1002/advs.202200622.

[175] P. Shi, J. Ma, M. Liu, S. Guo, Y. Huang, S. Wang, L. Zhang, L. Chen, K. Yang, X. Liu, Y. Li, X. An, D. Zhang, X. Cheng, Q. Li, W. Lv, G. Zhong, Y.-B. He, F. Kang, A Dielectric Electrolyte Composite with High Lithium-ion Conductivity for High-voltage Solid-State Lithium Metal Batteries, Nat. Nanotechnol. 18 (2023) 602–610, https://doi.org/10.1038/s41565-023-01341-2.

[176] M. Si, D. Wang, R. Zhao, D. Pan, C. Zhang, C. Yu, X. Lu, H. Zhao, Y. Bai, Local Electric-Field-Driven Fast Li Diffusion Kinetics at the Piezoelectric $LiTaO_3$ Modified Li-Rich Cathode–Electrolyte Interphase, Adv. Sci. 7 (2020) 1902538, https://doi.org/10.1002/advs.201902538.

[177] P. Zou, R. Zhang, L. Yao, J. Qin, K. Kisslinger, H. Zhuang, H.L. Xin, Ultrahigh-Rate and Long-Life Zinc–Metal Anodes Enabled by Self-Accelerated Cation Migration, Adv. Energy Mater. 11 (2021) 2100982, https://doi.org/10.1002/aenm.202100982.

[178] Y. Wang, J. Ju, S. Dong, Y. Yan, F. Jiang, L. Cui, Q. Wang, X. Han, G. Cui, Facile Design of Sulfide-Based all Solid-State Lithium Metal Battery: In Situ Polymerization within Self-Supported Porous Argyrodite Skeleton, Adv. Funct. Mater. 31 (2021) 2101523, https://doi.org/10.1002/adfm.202101523.

[179] H. Pan, M. Zhang, Z. Cheng, H. Jiang, J. Yang, P. Wang, P. He, H. Zhou, Carbon-free and binder-free Li-Al alloy anode enabling an all-solid-state Li-S battery with high energy and stability, Sci. Adv. 8 (2022) eabn4372, https://doi.org/10.1126/sciadv.abn4372.
[180] Z. Wang, Y. Cao, J. Zhou, J. Liu, X. Shen, H. Ji, C. Yan, T. Qian, Processing Robust Lithium Metal Anode for High-security Batteries: A Minireview, Energy Storage Mater. 47 (2022) 122–133, https://doi.org/10.1016/j.ensm.2022.01.049.
[181] J. Cao, Y. Shi, A. Gao, G. Du, M. Dilxat, Y. Zhang, M. Cai, G. Qian, X. Lu, F. Xie, Y. Sun, X. Lu, Hierarchical Li Electrochemistry using Alloy-type Anode for High-energy-density Li Metal Batteries, Nat. Commun. 15 (2024) 1354, https://doi.org/10.1038/s41467-024-45613-4.

Ming Liu, is currently pursuing a Ph.D. under the supervision of Prof. Zhipeng Ma at the School of Environmental and Chemical Engineering, Yanshan University. And is focusing on the design of (quasi-) solid-state electrolyte for inhibiting lithium-metal anode corrosion.

Ailing Song, Associate Professor and Master's supervisor at the School of Environmental and Chemical Engineering, Yanshan University. She completed her Ph.D. at Yanshan University in January 2021. From 2019 to 2021, she served as a visiting scholar at the University of Technology Sydney. Her research focuses on the design and development of highly stable advanced functional materials for energy storage and conversion applications.

Xinyi Zhang, is currently pursuing a M.Sc degree under the supervision of Prof. Xiujuan Qin at the School of Environmental and Chemical Engineering, Yanshan University. Her current research focuses on modification of lithium anode magnetic collector.

Jie Wang, is currently pursuing a M.Sc degree under the supervision of Prof. Zhipeng Ma at the School of Environmental and Chemical Engineering, Yanshan University. His current research focuses on preferentially deposition of lithium metal anode.

Yuqian Fan, Associate Professor and Master's supervisor at the School of Environmental and Chemical Engineering, Yanshan University, earned his Ph.D. in Chemistry from Zhejiang University, under the supervision of Academician Chu-Nan Cao. His main research areas include the development of advanced energy storage electrodes (for large-scale storage and metal-ion batteries), nickel-iron electroplating technology, lithium battery second-use and recycling technologies, and hydrogen production via water electrolysis.

Guoxiu Wang is the Director of the Centre for Clean Energy Technology and a Distinguished Professor at the University of Technology Sydney. Professor Wang is an expert in materials chemistry, electrochemistry, energy storage and conversion, and battery technologies. His research interests include lithium-ion batteries, lithium–air batteries, sodium-ion batteries, lithium–sulfur batteries, 2D materials, and electrocatalysis for hydrogen production. Professor Wang has published over 650 refereed journal papers with an h-index of 162. His publications have attracted over 86 000 citations. He has been recognized as a highly cited researcher in both Materials Science and Chemistry by Clarivate Analytics.

Hao Tian received his B.S. and M.S. from Lanzhou University in 2009 and 2012, his M.S. from the University of New South Wales in 2014, and his Ph.D. from Curtin University in 2018. He is a postdoctoral research associate at the Centre for Clean Energy Technology, University of Technology Sydney. His current research mainly focuses on the design and synthesis of nanostructured materials in the field of lithium-ion batteries, lithium-sulfur batteries, zinc-air batteries, electrocatalysis, thermal-catalysis and photocatalysis.

Zhipeng Ma, Professor and Ph.D. supervisor at the School of Environmental and Chemical Engineering, Yanshan University, obtained his Ph.D. in Industrial Catalysis from Yanshan University in January 2015. His research focuses on the development of high-energy power batteries and large-scale energy storage technology applications. He has led two National Natural Science Foundation projects and received recognition as a top young talent in Hebei province.

Guangjie Shao, Professor and Ph.D. supervisor at the School of Environmental and Chemical Engineering, Yanshan University, primarily focuses on electrochemical energy and green energy storage technology applications. He has led and participated in National Natural Science Foundation projects and Hebei Provincial Innovation Research Group projects. His primary research interests focus on addressing critical technical challenges associated with supercapacitors, metal-ion batteries, metal-sulfur batteries, electrocatalysis, and developing high-gravity electrodeposition technology, and nanostructured materials.